

Earth Radiation Budgets

G. L. STEPHENS,¹ G. G. CAMPBELL, AND T. H. VONDER HAAR

Department of Atmospheric Science, Colorado State University, Fort Collins, Colorado 80523

This paper presents the annual and seasonal averaged earth atmosphere radiation budgets derived from the most complete set of satellite observations available in late 1979. The budgets are derived from a composite of 48 monthly mean radiation budget maps. The annual, global average emitted infrared flux is 234 W m^{-2} , planetary albedo is 0.30, and the net flux is zero within measurement uncertainty. The annual cycle of net flux is also studied in detail, and the observed globally averaged net flux displays an annual cycle that is of similar magnitude and phase to the annual cycle imposed by the influence of sun-earth distance variations on solar radiation input into the atmosphere. A study of the geographical distribution of the annual variability of the net flux reveals that generally greater than 95% of this variability occurs as a result of the semi and annual cycles that may be forced by the regular variation of solar declination throughout the year. However, the amounts of energy contained in the variance from year to year is large. Thus, we direct radiation modeling studies to these regions and situations where the potential for climate impact due to radiation budget variability is the greatest. The individual components of emitted flux and planetary albedo display expectedly more high-frequency variability particularly equatorward of 30° latitude governed by weather features and their attendant cloud distributions. Radiative transfer model simulations of the observed budget quantities at the 'top-of-the-atmosphere' are good at least for the zonally averaged case. Significant differences exist between the present surface radiation budget calculations and those previously estimated. The differences, largely a result of the exclusion of enhanced absorption in the window region ($8\text{-}14 \mu\text{m}$) in earlier budget calculations, provide some 35 W m^{-2} more radiant energy into the oceans in the tropics than previously estimated. The validity of this result was verified by using GATE radiation budget measurements.

1. INTRODUCTION

The earth's radiation balance has been a subject of a number of studies for many years. Crucial to the question of climate research is the knowledge of the solar radiation input and the longwave radiation output at the top of the atmosphere and the exchange of heat, momentum, and material (especially water vapor) at the bottom. Furthermore, it is necessary to know the size and scale of interannual variations in the components of the energy budget. It is particularly important to assess the role of oceans in climatic variations and the extent and variability of the partitioning of the heat transport between the atmosphere and the oceans. It is evident that accurate and extensive measurements of the earth's radiation budget are required particularly over a period of several years to provide insight as to the extent of the interannual variabilities. Satellite measurements presently provide the best estimate of the earth radiation budget with sufficient temporal and spatial resolution over the entire globe. Further, from a combination of such data with conventional measurements of atmospheric and oceanic variables, the heat transports within the ocean and atmosphere can be deduced [e.g., Oort and Vonder Haar, 1976].

A number of studies have been presented over the last 10–15 years regarding the mean steady state magnitudes of the energy exchange between earth and space. For example, Vonder Haar and Suomi [1971] presented results for the mean annual and seasonal cases based on measurements during 5 years (1962–1966). Others, including Winston [1967] and Raschke and Bandeen [1970] discussed short spans of data (weeks and seasons). Raschke *et al.* [1973] reported on budget results from measurements obtained from an experiment on the Nimbus 3 satellite. In this paper the earth atmospheric radiation budgets are presented for a composite of 48 months

over an intermittent period spanning 14 years (1964–1977) including 24 months of the more recent Nimbus 6 data obtained from the continuing earth radiation budget (ERB) experiment. The reported data are a result of a continuing compilation of radiation budget measurements that were first reported by Ellis and Vonder Haar [1976] (29 months of selected radiation budget measurements).

This paper provides mean annual and seasonal radiation budgets determined with the composite satellite data set and describes the errors associated with the data. The intermittent nature of the composite data set presented here perhaps prohibits detailed studies of the interannual variability of the radiation budget. However, a reasonable estimate of the annual variability of the radiation budget is presented.

The determination of the radiative balance at the earth's surface is also essential to atmospheric modeling, and, in particular, surface radiation budgets may provide insight into the possible atmospheric and oceanic partitioning of the heat transport. This paper presents calculated surface budgets, using a radiative transfer model. Comparisons between the current budget calculations and previous calculations are presented to highlight major differences arising from advances in our knowledge of radiative transfer in the atmosphere. Furthermore, the calculations are compared to the satellite-derived radiation budgets. Satellite-based observations of the components of the radiation budget currently serve as one of the important tests of radiation modeling validity.

2. SATELLITE DATA SOURCES

a. Suitability of Various Satellite Measurements for Radiation Budget Determinations

There is an increasing amount of information on the planetary radiation budget being provided by satellite measurements. Thus, the possibility arises for misunderstanding the different measurements as a source of data for energy budget studies. It is important for scientists who use the data to understand the nature of the measured or estimated quantities before the data can be interpreted for energy budget and cli-

¹ On leave from CSIRO, Division of Atmospheric Physics, Aspendale, Victoria, Australia.

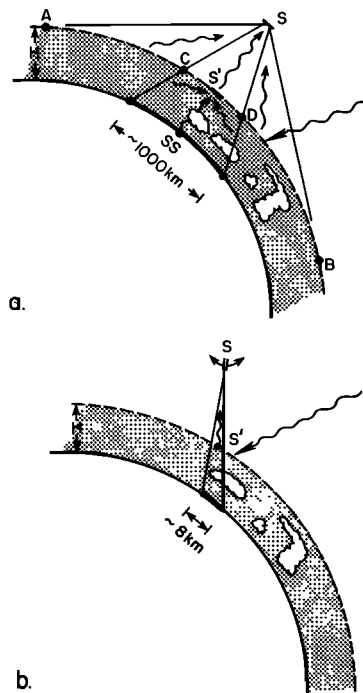


Fig. 1. Schematic representation of the measured quantities by (a) a flat plate and (b) scanning detector.

mate-related studies. Ideally, radiation budget studies require measurements at the 'top of the atmosphere' of the total upwelling radiant energy from the earth atmosphere system, that is, the total radiant energy in both the solar and IR spectra integrated over all directions. No satellite measurement system yet developed can completely accommodate these rather fundamental requirements, but some provide better approximations than others. Furthermore, quantitative estimates of the uncertainties associated with the different systems vary in detail.

There are basically two fundamentally different sensors employed to measure the upwelling solar and IR radiation leaving the earth atmosphere system: radiometers that employ flat plate sensors and scanning radiometers. The measured quantities derived from these instruments are as fundamentally different as the instruments themselves. This point is evident from Figure 1, which schematically depicts the nature of the measurement and of the region sampled by the instrument.

The flat plate sensor measures the upwelling radiant flux density (exitance) reaching the plate and includes the earth atmosphere signal from a well-defined cone (SAB). The object is to convert this measurement at the satellite altitude (S) to an equivalent flux measurement at height H (the top of the atmosphere). The upwelling radiation at S , while composed of radiation from within cone SAB, originates largely within the smaller cone SCD. This more confined sampling region is a consequence of the instrument weighting radiation received about the subsatellite point (SS) more heavily than radiation received from those regions toward the limb. This feature is one of the determinants of the practical instrument resolution ($\sim 10^\circ$ ground coverage area for the flat plate sensors in orbits of height ~ 600 km).

The satellite-based detector at S measures not only the radiant energy through the 'equivalent detector' at S' but also radiation received from the surrounding regions of the atmosphere. Thus some correction is strictly required to eliminate this radiation so that the exitance measured at S represents

the exitance at S' . However, since the radiation through S' accounts for a large amount of the total upwelling radiant energy detected at the satellite, this correction is likely to be small. Finally, since spatial gradients or time rates of change of the radiation budget are often the important parameters under consideration and the spatial and temporal differences of measurements of the radiation through S are very similar to those through S' , the data at satellite altitude are often employed without adjustment.

The scanning radiometer, on the other hand, measures the radiant energy (analogous to radiance) confined to a particular direction and to a small but finite solid angle (Figure 1b). Thus while the reinterpretation of this measurement at S' is trivial, such a measurement does not represent the total upwelling radiant energy but is rather the energy sampled in a confined but small set of solid angles.

It is obvious from the comparisons shown in Figures 1a and 1b that the flat plate sensor, while encompassing a majority of the total upwelling radiation, does so at the expense of ground resolution. The full field of view is $\sim 60^\circ$ but the effective resolution is of the order of 10° (or ~ 1000 km) resulting in a smoothing of the data. Scanning radiometers, by contrast, have far better resolution (often $<2^\circ$ with averaging) but at the expense of losing representation of the total radiant exitance from the earth-atmosphere.

The angular variation of the radiation field measured with a scanner is most severe when applied to the determination of planetary albedo. While the problem still exists for IR measurements, it is generally assumed that the emitted radiation has approximate black body characteristics and is therefore more nearly isotropic. Generally, each satellite measures radiation $N(\Theta_{\text{obs}}, \psi_{\text{obs}}, \Theta_0)$, which is a function of the solar zenith angle Θ_0 (for solar radiation only), satellite zenith angle Θ_{obs} , and the relative azimuth ψ_{obs} . The 'measured' instantaneous albedo is usually estimated by

$$\alpha_m(\Theta_{\text{obs}}, \psi_{\text{obs}}, \Theta_0) = \pi N(\Theta_{\text{obs}}, \psi_{\text{obs}}, \Theta_0) / Q \cos \Theta_0 \quad (1)$$

where Q is the incident extraterrestrial solar irradiance. In this case, α_m is an isotropic albedo (i.e., an albedo determined assuming $N(\Theta, \psi, \Theta_0)$ is isotropic). This is not a planetary albedo that is of the form

$$\alpha(\Theta_0) = \left[\int_0^{2\pi} \int_0^1 N(\Theta, \psi, \Theta_0) \cos \Theta d\psi d\Theta \right] / Q \cos \Theta_0 \quad (2)$$

and involves an integration of the upwelling radiance over all directions for the given solar zenith angle. Thus, albedo estimates by the scanning radiometer strictly require integration of the form of (2). To convert α_m to α it is necessary to introduce a suitably defined function $\rho(\Theta, \psi, \Theta_0)$ characterizing the variation of radiance with the angular directions Θ , ψ , and Θ_0 . This function is usually introduced as a ratio of the integrated anisotropic radiance (i.e., irradiance) to the 'isotropic' irradiance $\pi N(\Theta_{\text{obs}}, \psi_{\text{obs}}, \Theta_0)$ via

$$\rho(\Theta_{\text{obs}}, \psi_{\text{obs}}, \Theta_0) = \frac{\int_0^{2\pi} \int_0^1 N(\Theta, \psi, \Theta_0) \cos \Theta d\psi d\Theta}{\pi N(\Theta_{\text{obs}}, \psi_{\text{obs}}, \Theta_0)} \quad (3)$$

allowing an estimate of albedo via

$$\alpha(\Theta_0) = \frac{\pi N(\Theta_{\text{obs}}, \psi_{\text{obs}}, \Theta_0) \rho(\Theta_{\text{obs}}, \psi_{\text{obs}}, \Theta_0)}{Q \cos \Theta_0} \quad (4)$$

TABLE 1. Satellite Systems

COMMENT	NIMBUS 6	NOAA (TIROS N)	GOES, SMS	NIMBUS 7	ERBE (1983)
ORBIT	Sun-synchronous polar orbiting		Geosynchronous orbit	Polar orbiting Sun synchronous	2 sun synchronous 1 Drifter orbiter
DETECTOR	Flat Plate	Single axis scanners		Flat Plate	Multi axis scanner Single axis scanner
INTEGRATION OVER DIRECTION	Largely eliminated (except in polar regions)	Requires a ρ model		By scanning in more directions, ρ may be explicitly determined	Requires a ρ model (hopefully from Nimbus 7 for example)
INTEGRATION OVER WAVELENGTH	Broadband detectors solar (0.2-0.38) IR (3.8->50)	Requires empirical corrections to broadband values		Both radiometers are broadband instruments	
RESOLUTION	Coarse resolution ($\sim 10^\circ \times 10^\circ$) with smoothing	High Resolution ($\sim 2^\circ \times 2^\circ$) or higher		Flat Plate have coarse resolution Scanner ($\sim 4^\circ \times 4^\circ$)	Scanner ($\sim 2^\circ \times 2^\circ$)
DIURNAL SAMPLING	Measurement at single daylight hour ($\sim 0Z, 12Z$)	Measurement twice daily (0900, 2100 local time)	Continuous temporal sampling	As for Nimbus 6 (0Z, 12Z)	Improved temporal sampling with 3 polar orbiting satellites six times a day

The function ρ , or any similarly defined function, is often known as a bidirectional (or biconical) reflectance model and is determined largely by cloud cover, cloud type, surface conditions, etc. The behavior of ρ as a function of the angles Θ , ψ , and Θ_0 is still very poorly known for all but simple surfaces (e.g., oceans). Intuitively, the variation of ρ with the directional angles is considerable, especially over snow and ice surfaces. The behavior of ρ in cloud regions is still largely unknown, but it may be highly variable for different cloud conditions. For example, the reflection from cloud layers as a function of emergent zenith angle is extremely variable with limb brightening for layer clouds [Liou, 1973] and limb darkening for broken or finite clouds [McKee and Cox, 1976]. Furthermore, the behavior of ρ with the designated angles is spectrally dependent. For example, reflectance by clouds in the visible region in which there is supposedly little absorption is quite different than reflectance in the near IR region where large absorptions are possible. This effect may be even more significant for precipitating clouds [Welch et al., 1980] and in regions of high ice clouds [Stephens, 1980]. The spectral variation of ρ is also likely to be significant when applied to other surfaces (e.g., snow, Wiscombe and Warren [1980]).

The determination of the mean daily albedo then involves an integration of $\alpha(\Theta_0)$ with respect to Θ_0 , which requires the application of directional reflectance models (i.e., directional reflectance). The behavior of α with varying solar zenith angles Θ_0 is a function of the type of reflecting surface.

The performance, in terms of applicability to radiation budget estimates, of the various satellite measuring systems is summarized in Table 1. Five major systems are reviewed, the sun-synchronous polar orbiter like Nimbus 6 and 7 and NOAA satellites, geosynchronous satellites (e.g., GEOS, SMS), and the proposed ERBE program (1984), which is to implement three polar orbiting satellites. The local times of sampling are also shown in parentheses in the section labeled diurnal variation.

The flat plate sensors associated with the Nimbus 6 and 7 satellites have significant advantages in that measurements are broad band (i.e., they measure the upwelling solar radiation in the spectral region from 0.2 to 3.8 μm and the IR emitted flux for the spectral region 3.8 to $> 50 \mu\text{m}$) and also measure radiant energy integrated over a broad variation of angles. Unfortunately, the satellite sun-synchronous orbits do not pass directly over the polar regions, and the earth's radiation viewed from those regions by flat plate sensors is at some oblique angle. Therefore, the determination of planetary albedo in the polar regions (poleward of about 70° latitude) is subject to some uncertainty since it requires large angular correction, the validity of which remains uncertain. The chief disadvantages of these measurements are their inherent coarse resolution and the possibility of diurnal bias. Possible diurnal biases in reflectance by varying solar elevation can be corrected as discussed above (i.e., some average of $\alpha(\Theta_0)$ is performed [e.g., Raschke et al., 1973]). However, it must be recognized that this data processing cannot remove possible diurnal effects that arise from variations in the state of the atmosphere (such as cloud cover). In particular, the tropics that constitute roughly half of the surface area of the earth and account for more than half of the radiative interaction with space, exhibit some fairly regular variations in temperature and cloudiness over the diurnal cycle [Riehl and Miller, 1978; Short and Wallace, 1980].

The scanning radiometers (SR) employed on the NOAA and geosynchronous satellites measure the upwelling radiation in narrow spectral regions (0.5-0.7 μm in the visible and 10.5-12.5 μm in the IR). The disadvantage of such measurements is the need to correct empirically these narrow spectral band values to broad band total shortwave and longwave radiant energies. A regression approach is employed to the IR measurements from the NOAA scanning radiometer [Gruber and Winston, 1978], which provides representative values of emitted flux. A similar correction is needed for the shortwave

TABLE 2. Chronological List of Earth Orbiting Satellites From Which Present Radiation Measurements Were Taken

Month	Season	1964	1965	1966	1968	1969	1970	1975	1976	1977	Sample Size
Jan.	DJF		Ex(1030)			E7	N3		N6	N6	5
Feb.	DJF		Ex(1035)			E7			N6	N6	4
March	MAM		Ex(1040)			E7			N6	N6	4
April	MAM					N3(1130)*			N6	N6	3
May	MAM					N3			N6	N6	3
June	JJA			N2(1130)*		N3			N6	N6	4
July	JJA	Ex(0830)				N3		N6(1145)*	N6		4
Aug.	JJA	Ex(0855)				N3		N6	N6		4
Sept.	SON	Ex(0915)							N6	N6	3
Oct.	SON	Ex(0940)			E7(1430)	N3		N6	N6		5
Nov.	SON	Ex(1005)				E7			N6	N6	4
Dec.	DJF	Ex(1030)		E3(1440)	E7				N6	N6	5
Annual		6	3	2	3	9	1	6	12	6	48

The approximate local time at which each satellite crossed the equator during daylight hours appears in parenthesis. EX, experimental; N2, Nimbus 2; N3, Nimbus 3; N6, Nimbus 6; E3, ESSA 3; E7, ESSA 7.

Resolution = half power diameter: Experimental, 1280 km, 11.5°; ESSA3; Nimbus 2, averaged to 10° grid; ESSA7, 2200 km, 20°; Nimbus 3, averaged to 10° grid; Nimbus 6, 1100 km, 10° (analyzed from 16°).

*Albedo corrected for diurnal variation of reflection with directional reflectance model.

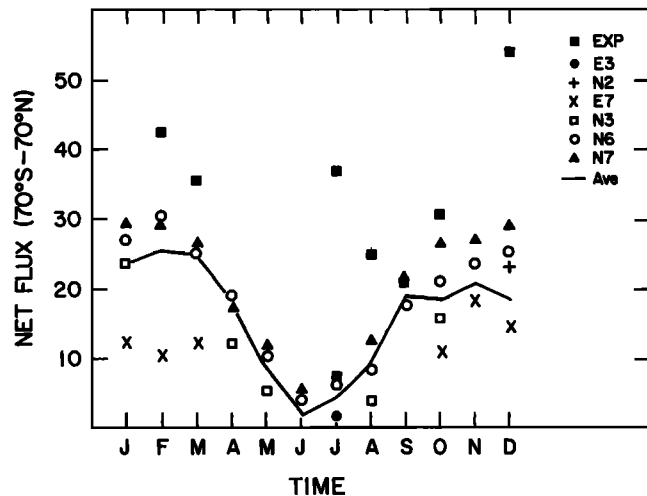
measurements, but it is not performed for the current scanning radiometer 'albedo' estimates. Another significant disadvantage is the need to correct the measurements for angular variation of the radiance fields to provide ultimately the integral quantity in (3). Again this correction is not employed to the currently available scanning radiometer data.

The advantages associated with the scanning radiometer data reside in the high resolution of the data that are available over a longer 'continuous' period than are the flat plate measurements. Future Tiros and NOAA SR data will be available at 0730, 1500, 1930, and 0300 (local time), which may eliminate diurnal biases. Studies of any diurnal cycle evident in the radiation budget data, however, are best suited to geosynchronous satellite data, and such studies are required to test the extent of possible diurnal biases that may occur in the sun-synchronous polar orbiting satellites. Unfortunately, the measurements from geosynchronous satellites are not global in extent, and the data also require the difficult angular and spectral corrections described above for the SR.

In addition to the flat plate sensors, the Nimbus 7 satellite has a multi-axis broad band scanning radiometer that not only measures the upwelling radiance field across the entire spectrum but also scans for a number of different angles. This data, presently being processed, may offer significant advances to our present qualitative understanding of the bidirectional reflectance function. Data from the existing single axis scanning radiometers can also be employed to study this function but for a more restricted variation of the dependent angles (e.g., θ , ψ , and θ_0 in (2)). The proposed ERBE program will employ two near polar-orbiting sun-synchronous satellites and another with orbital inclination of 48° as an attempt to overcome the possible diurnal biases associated with the current measurements. The program will continue its use of the flat plate sensors as well as employing a broad band single axis scanning radiometer. It is hoped by the time of those measurements that the current scanning radiometer data from Nimbus 7 as well as the current single axis scanner measurements will lead to a workable understanding of the bidirectional reflectance function.

TABLE 3. The Standard Deviation of the Net Radiation for January, April, July, and October

Latitude	January	April	July	October
90°–80°N	4	8	10	5
80°–70°N	4	9	8	4
70°–60°N	4	9	7	5
60°–50°N	4	9	7	5
50°–40°N	5	9	7	6
40°–30°N	6	10	7	7
30°–20°N	7	10	7	7
20°–10°N	7	10	7	7
10°–0°N	7	9	6	7
0°–10°S	7	9	7	7
10°–20°S	7	10	7	7
20°–30°S	7	10	7	7
30°–40°S	7	9	5	7
40°–50°S	7	8	5	6
50°–60°S	7	8	5	6
60°–70°S	8	7	4	6
70°–80°S	9	5	4	6
80°–90°S	10	4	3	5

Fig. 2. Experimental comparisons for the net flux (W m^{-2}) as a function of time.

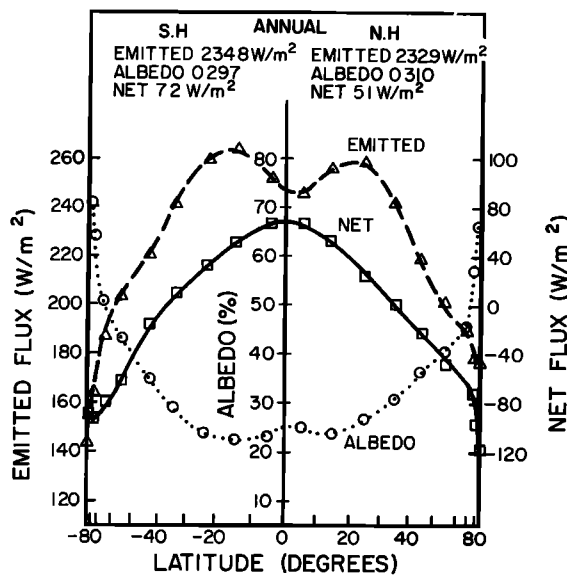


Fig. 3a. Zonally averaged profiles of the annually averaged emitted flux, net flux, and planetary albedo.

rectional reflectance function. Such a reflectance model may then be coupled to the scanning radiometer data to provide high resolution radiation budget estimates.

b. Satellite Data and Error Estimates

Data from satellite measurements of the reflected shortwave (planetary albedo), emitted longwave, and net radiative fluxes have been compiled into global radiation budget climatologies. The measurements from six different experiments comprise the composited data presented in this paper. Table 2 is a chronological summary of the satellite radiation budget data including the sample size in terms of months, seasons, and years. The measurements were of variable accuracy and resolution, and the diameter of the half power region, indicative of the spatial resolution of the particular experiment, is included in the table. The 48-month set is a selective compilation of most of the satellite measurements at that time. All satellites were in a sun-synchronous orbit sampling at near one

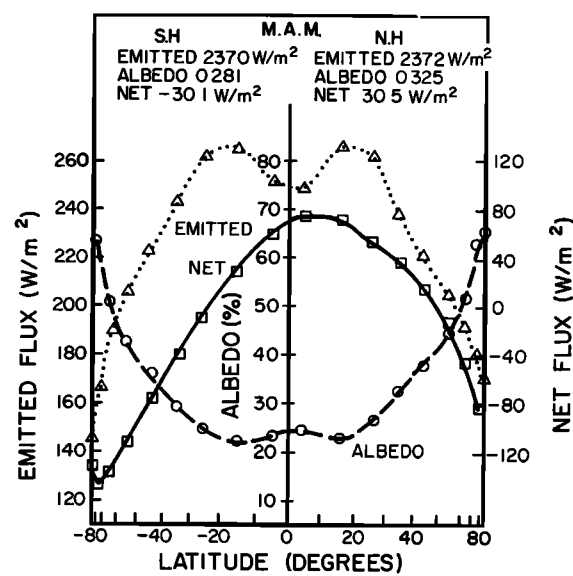


Fig. 3c. Same as for Figure 3b but for MAM.

local time during daylight hours (which is also included in Table 2).

The values of net radiation contain certain systematic errors. Some of the major sources of these systematic errors, concerning measurements, were discussed above but also should include the related problems with calibration of the sensors and the degradation of the sensor in space. In addition, these uncertainties are augmented by the natural variability of the system, that is, the natural year to year variability effects the climatological averages when the number of samples are small. It is extremely difficult to assign quantitative estimates to these uncertainties. Table 3 is included to present the standard deviations of the monthly means of the net radiation and may be considered an indicator of total uncertainty. These are presented for the 4 months shown in the table and suggest that the total uncertainty in net radiation is of the order of 10 W m^{-2} .

The data employed in the study and summarized in Table 2

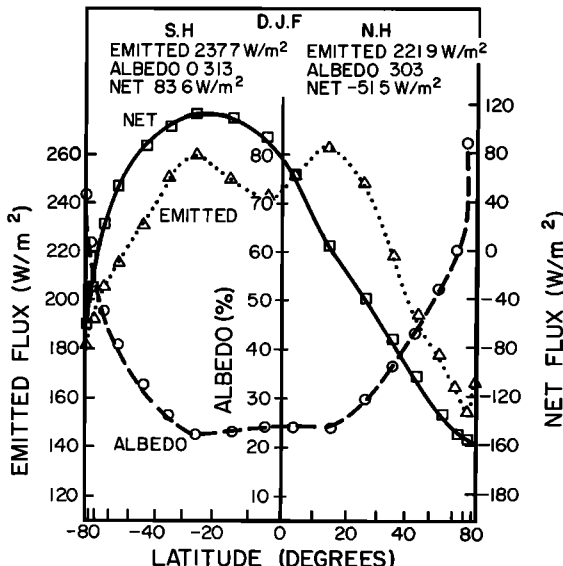


Fig. 3b. Same as for Figure 3a but for the designated DJF season.

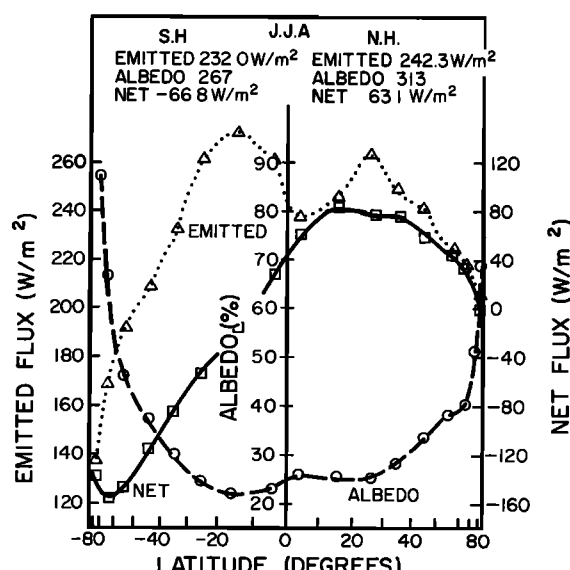


Fig. 3d. Same as for Figure 3b but for JJA.

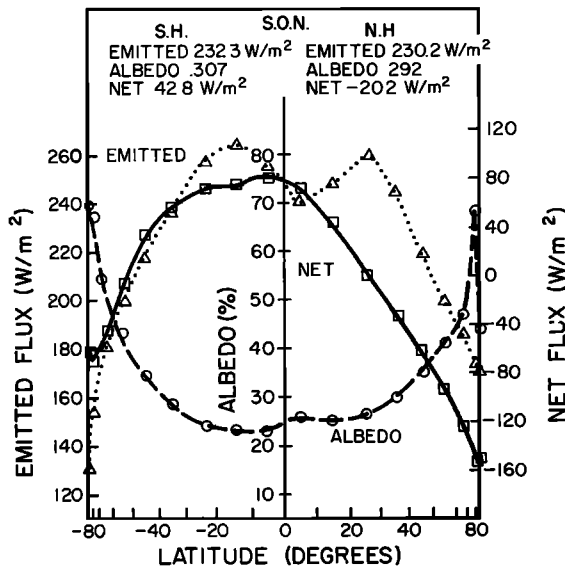


Fig. 3e. Same as for Figure 3b but for SON.

before 1971 are essentially from *Ellis and Vonder Haar* [1976] for medium resolution radiometers or wide angle flat plate disc sensors. The 24 months of Nimbus 6 data (July 1975 to June 1977) are obtained from wide angle and broad band sensors of the earth radiation budget experiment (ERB). Figure 2 displays the area mean from 70°N to 70°S of net flux as a function of time with observations from the individual instruments superimposed. (Because of missing data near the poles from some experiments, the area average was not carried out for global averages.) The results suggest that the variations around the mean (shown as a solid curve) are likely to be a result of observing system differences and perhaps to a lesser extent due to atmospheric variability since the measurements from particular experiments generally lie to one side or another of the mean. The observations from Nimbus 6 and 7 that supply half of the present data set are very similar, while the results from the experimental satellite are substantially different. There are no obvious reasons for rejecting the results from the experimental satellite. The systematic differences may, in part, be a result of different sampling period for that satellite (see Table 2). The annual global average emitted

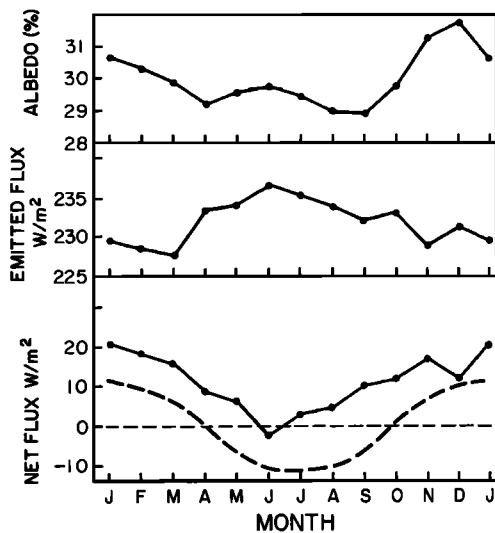


Fig. 4. Components of the global radiation balance of the earth. Shown are the planetary albedo, longwave flux to space, and the net radiative flux. Included also with the net flux is the variation induced only by varying earth-sun distances (dashed curve).

radiant exitance is $234 \pm 7 \text{ W m}^{-2}$, the albedo is 0.30 ± 0.01 (shown in Figure 3a) and the net radiation is $9 \pm 10 \text{ W m}^{-2}$. The small positive net flux value for the annual average is indicative of the absolute magnitude of the error associated with the net flux determinations. While the absolute error is of the order of 10 W m^{-2} , the relative error (and thus gradients of net flux) is much smaller [Campbell and Vonder Haar, 1980].

3. RADIATION BUDGET MEASUREMENTS

The planetary net radiation budget is composed of incoming solar flux, reflected solar flux to space, and the emitted terrestrial flux. At the top of the earth atmosphere boundary, the net radiation budget is defined as

$$N = (1 - \alpha)Q - I \quad (5)$$

where α is the planetary albedo, Q is the incoming solar flux based on the solar constant of 1376 W m^2 [Hickey et al., 1980] and corrected for variations in sun earth distance, day length, and solar declination and I is the emitted flux (IR) by the

TABLE 4a. Zonal Mean Emitted Radiant Exitance W/m^2

Latitudes, deg.	1	2	3	4	5	6	7	8	9	10	11	12	Annual		
1	90	80	165	155	146	173	189	207	207	199	178	170	163	177	177
2	80	70	157	149	154	183	197	211	212	207	186	175	160	156	179
3	70	60	165	164	170	196	208	221	224	217	198	186	173	167	191
4	60	50	175	177	188	204	213	222	228	224	211	200	188	182	201
5	50	40	191	194	203	216	226	235	244	243	232	220	205	198	217
6	40	30	217	218	224	235	241	254	259	263	253	247	231	222	239
7	30	20	250	248	251	265	266	268	262	261	261	263	253	251	258
8	20	10	266	264	261	270	260	251	241	236	242	250	251	259	254
9	10	0	251	251	248	240	232	233	233	235	235	244	242	250	241
10	0	-10	240	240	240	243	257	261	261	261	260	257	248	246	251
11	-10	-20	248	247	250	264	270	273	272	276	271	266	257	253	262
12	-20	-30	261	256	254	263	258	260	260	264	259	258	256	262	259
13	-30	-40	253	251	244	239	233	229	231	232	233	238	239	249	239
14	-40	-50	232	232	225	217	213	209	205	207	211	219	220	229	218
15	-50	-60	217	217	208	204	199	195	188	187	192	201	208	216	203
16	-60	-70	209	204	193	186	177	172	164	161	165	180	197	209	185
17	-70	-80	196	184	165	153	146	146	131	124	128	151	183	200	159
18	-80	-90	187	171	148	121	105	110	104	94	94	126	170	190	135
	90	-90	230	228	228	233	234	236	235	235	232	233	229	231	232

TABLE 4b. Zonal Mean Albedo, Percent

Latitudes, deg.	1	2	3	4	5	6	7	8	9	10	11	12	Annual	
1	90	80	I*	I*	69	58	69	75	69	60	44	I*	I*	67
2	80	70	I*	83	69	63	62	54	50	49	66	77	I*	57
3	70	60	78	56	55	54	49	42	39	40	42	51	64	46
4	60	50	56	50	49	42	40	39	38	38	37	43	49	41
5	50	40	46	43	40	36	34	35	33	32	33	34	39	36
6	40	30	37	36	34	32	30	28	27	26	29	29	33	31
7	30	20	30	29	27	25	25	25	26	26	26	26	28	26
8	20	10	24	23	22	20	22	24	26	26	27	25	26	24
9	10	0	24	24	24	24	26	26	26	26	26	25	26	25
10	0	-10	25	24	24	24	21	22	23	23	22	23	24	23
11	-10	-20	24	23	23	22	21	21	22	22	22	23	24	23
12	-20	-30	23	24	23	24	24	24	25	25	25	25	24	24
13	-30	-40	27	28	29	29	30	30	30	30	29	29	28	29
14	-40	-50	33	34	34	37	38	39	39	36	35	34	33	35
15	-50	-60	41	41	40	42	44	47	48	45	43	44	43	42
16	-60	-70	46	47	46	54	62	72	77	65	56	56	52	49
17	-70	-80	61	62	61	86	I*	I*	I*	88	79	65	66	64
18	-80	-90	70	72	40	I*	I*	I*	I*	80	67	75	75	70
	90	-90	31	30	30	29	30	30	29	29	30	31	32	30

* Refers to dark or missing.

earth atmosphere system. The following analysis presents composited measurements of the quantities N , α , and I .

a. Zonal Radiation Budgets

The latitudinal distribution of the annual and seasonal net radiative energy input into the earth atmospheric system, the planetary albedo, and the outgoing (emitted) longwave radiation are shown in Figures 3a-3e for the 48-month composite data set as a function of latitude. (The abscissa scale is non-linear with respect to latitude but linear with respect to area.) In the annual profiles, approximate symmetry in N , α , and I prevails between the northern and southern hemispheres. The minimum in emitted flux near the equator (5°N) is a result of the high topped clouds associated with the ITCZ. It is apparent from the seasonal profiles how this minimum migrates about the equator. The high emission around 25°S and 25°N are indicative of the subtropical dry zones (both over land and over ocean). The annual profile of planetary albedo, on the other hand, displays a maximum at 5°N in concert with the minimum in the emitted flux. In the tropical region, the planetary albedo variation is influenced more by weather disturbances and their attendant cloud distributions. In the polar re-

gions, the major ice sheets are regions of large negative net radiation due to the high albedo of snow and ice. The general increase of albedo poleward of the subtropics is also partially attributable to the decreasing mean solar elevation angle with latitude.

The qualitative features of the seasonal net flux profiles displayed in Figure 3 show a maximum net radiative input in the tropics that migrates according to the sun's position and a net deficit of radiative energy in the polar regions. Also shown in Figure 3 are the hemispheric and global averages of the emitted flux, albedo, and net flux.

In Tables 4a-4c the zonally averaged values of emitted flux, planetary albedo and net flux are tabulated for each of the 12 months.

b. Annual Variations

There is a significant amount of month to month variation in the radiation budget quantities. This is exemplified in Figure 4, which shows the annual variation of the mean values of emitted flux, planetary albedo, and net flux (also shown in Figure 2). These values are area means from 70°N to 70°S . Global integrations were not performed in this case because

TABLE 4c. Zonal Mean Net Flux, W/m^2

Region, deg	1	2	3	4	5	6	7	8	9	10	11	12	Annual		
1	90	80	-165	I*	-132	-70	-55	-77	-61	-74	-126	I*	-163	-177	-118
2	80	70	I*	-146	-121	-84	-36	19	18	-46	-136	-166	I*	-156	-97
3	70	60	-158	-130	-92	-53	8	60	52	-10	-74	-136	-162	-164	-72
4	60	50	-142	-104	-64	0	54	73	57	13	-38	-103	-142	-156	-46
5	50	40	-112	-70	-23	37	77	81	70	37	-11	-65	-106	-129	-18
6	40	30	-81	-39	8	52	87	92	86	58	13	-36	-77	-97	6
7	30	20	-50	-9	35	64	85	86	84	70	41	-3	-41	-63	25
8	20	10	-3	31	67	86	92	90	88	88	76	46	11	-13	55
9	10	0	52	71	86	92	83	73	74	81	87	73	56	38	72
10	1	-10	95	100	94	74	44	24	27	48	74	84	88	85	70
11	-10	-20	113	106	81	35	-4	-28	-21	4	47	80	101	108	52
12	-20	-30	122	96	54	-3	-47	-70	-62	-29	25	74	113	124	33
13	-30	-40	117	72	21	-36	-81	-100	-92	-53	6	60	109	126	12
14	-40	-50	102	46	-12	-77	-121	-137	-124	-85	-25	35	94	116	-16
15	-50	-60	70	8	-47	-115	-153	-166	-153	-118	-63	-8	51	83	-51
16	-60	-70	46	-25	-81	-145	-167	-169	-160	-139	-94	-51	13	52	-77
17	-70	-80	-8	-71	-110	-149	I*	-146	I*	-123	-109	-65	-36	-7	-92
18	-80	-90	-35	-89	-99	I*	-105	-110	-104	I*	-69	-56	-57	-54	-83
	90	-90	21	18	16	9	6	-2	3	4	10	12	17	12	9

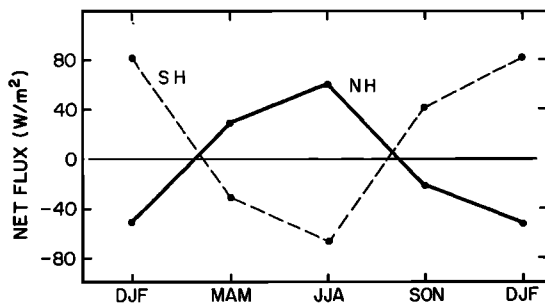


Fig. 5. The mean seasonal hemispheric net fluxes.

some data were missing poleward of 70°N and S for individual months. The annual cycle in the globally integrated net flux, previously reported by *Ellis et al.* [1978], has an amplitude (peak to peak) of about 26 W m^{-2} . The credibility of such a cycle can be qualitatively assessed from the heat budget studies of *Ellis et al.*, who showed that the change of heat content (storage) of the earth possessed similar amplitudes and phases to the planetary net flux. Their global heat storage estimates were computed by independent in situ measurements of temperature.

Shown on Figure 4 as a dashed curve is the annual cycle in the globally averaged integrated solar flux that has a peak to peak amplitude of about 22 W m^{-2} . This variation is a result only of external forcings associated with variations in the earth sun geometry. It is likely that the observed annual variation of the globally average net flux at the top of the atmosphere (solid curve in Figure 4) is largely a result of this external forcing. The residual of the cycle is likely to be a result of the hemispheric differences in land-ocean extent, but cloud cover differences between the hemisphere cannot be ruled out. Specifically, the annual cycle of planetary albedo is also likely to be determined by the hemispheric differences of snow ice extent that provides large albedos (particularly in the polar regions). Further, the annual variation in the longwave emission to space occurs in part because of unequal temperature responses between the land and the water surfaces and the asymmetrical distribution of these between the northern and the southern hemisphere.

Figure 5 presents the interannual variations of the hemispherically averaged net flux that are presented for the seasonal intervals specified above. For both hemispheres, the largest changes in the net flux from one season to another occur for the transition from solstice to equinox. This marked variation is also evident in the global maps of net flux discussed below.

c. Global Distributions

Figures 6–10 show the global distributions of emitted flux, planetary albedo, and net flux averaged for the mean annual and designated seasonal periods, respectively. The annual albedo maps reveal a distinct ocean continent contrast equatorward of 30°N and 30°S and the high reaching convective clouds associated with the Asian monsoon are particularly apparent especially when related to the low emission (less than 230 W m^{-2}) evident in Figure 6 for that region. Generally, a net radiation gain prevails over ocean regions that may be directly attributed to the lower albedo over oceans compared to the zonal average. Poleward of 30°N and S, the albedo is zonally uniform except for some slight continental influence (e.g., over North America) in the northern hemisphere.

A distinct feature of the net flux distribution is the relatively

high input of net radiative energy in the southeast Asian region and regions of relative low energy input particularly west of South America and southern Africa (associated with the presence of low persistent stratus clouds) and a minimum over the desert regions.

The maps presented in Figure 6 are for the mean annual case, and thus all daily and even seasonal anomalies are smoothed. Even so, at lower latitudes in particular, regions of relative gain and loss of energy are evident within a given zone. For example, distinct variations are evident in the net fluxes in the tropical zones where the deserts of Africa and Arabia appear as negative or small positive anomalies and the convective regions near Asia are large positive anomalies in net flux. Thus numerical simulations of the atmospheric or oceanic circulation cannot include forcing functions only as a function of latitude (i.e., of solar declination). *Stephens and Webster* [1979], for example, indicated that zonal variations in the radiative forcing cannot be simulated without zonal variations in cloud cover.

The albedos are generally negatively correlated with the emitted flux except over the desert regions discussed above. This reciprocity between emitted flux and albedo is a direct result of the effect of cloud on these components. Simply, the increased loss of energy to space by reflection from the cloud is offset by the decreased emission from the (colder) cloud tops. This reciprocity is evident in each of the seasonal maps producing net flux distributions that are more zonal in structure than either the maps of the two components α or I .

Other distinct features of the seasonal maps are the similarities of planetary albedo in the tropical regions for which a distinct ocean continent contrast is evident for all seasons. Second, there are three regions of significantly low emission (particularly for JJA) that contrast adjoining zones. These are located west of Panama, over the southern African continent, and in the southeast Asian region and are regions where cancellation between albedo and atmospheric emission do not cancel. For example, the net flux over the southeast Asian region displays a distinct net flux positive anomaly for most seasons but especially for MAM and JJA.

d. Variance in the Annual Cycle

As is evident in Figure 4, the global net flux, planetary albedo, and emitted flux display a distinct annual cycle. However, this annual cycle is more pronounced for a given region. For example, Figure 11 shows the annual cycle in net flux, emitted flux, and albedo for the southeast Asian region located at 70° – 80°E , 10° – 30°N . A study of the albedo cycle clearly indicates the distinct maximum associated with the height of the monsoon activity as measured by intensification of cloud amount. The emitted flux, by contrast, displays a pronounced minimum in concert with the albedo maximum. The combined effect is that the total energy reradiated to space is quite uniform despite the probable large change in cloudiness, and the annual cycle of net flux is similar to the cycle of solar radiation input (a function only of earth-sun geometry). The profiles shown in Figure 11 are a dramatic example of the reciprocity between the increased outgoing shortwave flux by reflection (i.e., a decreased shortwave absorption by the earth atmosphere system) and the decreased emission to space from the colder cloud tops.

From the 12 mean-monthly maps of net flux, we calculated maps of the amplitudes of both the annual and the semi-annual cycles (Figures 12a and 12b). Also shown in Figures

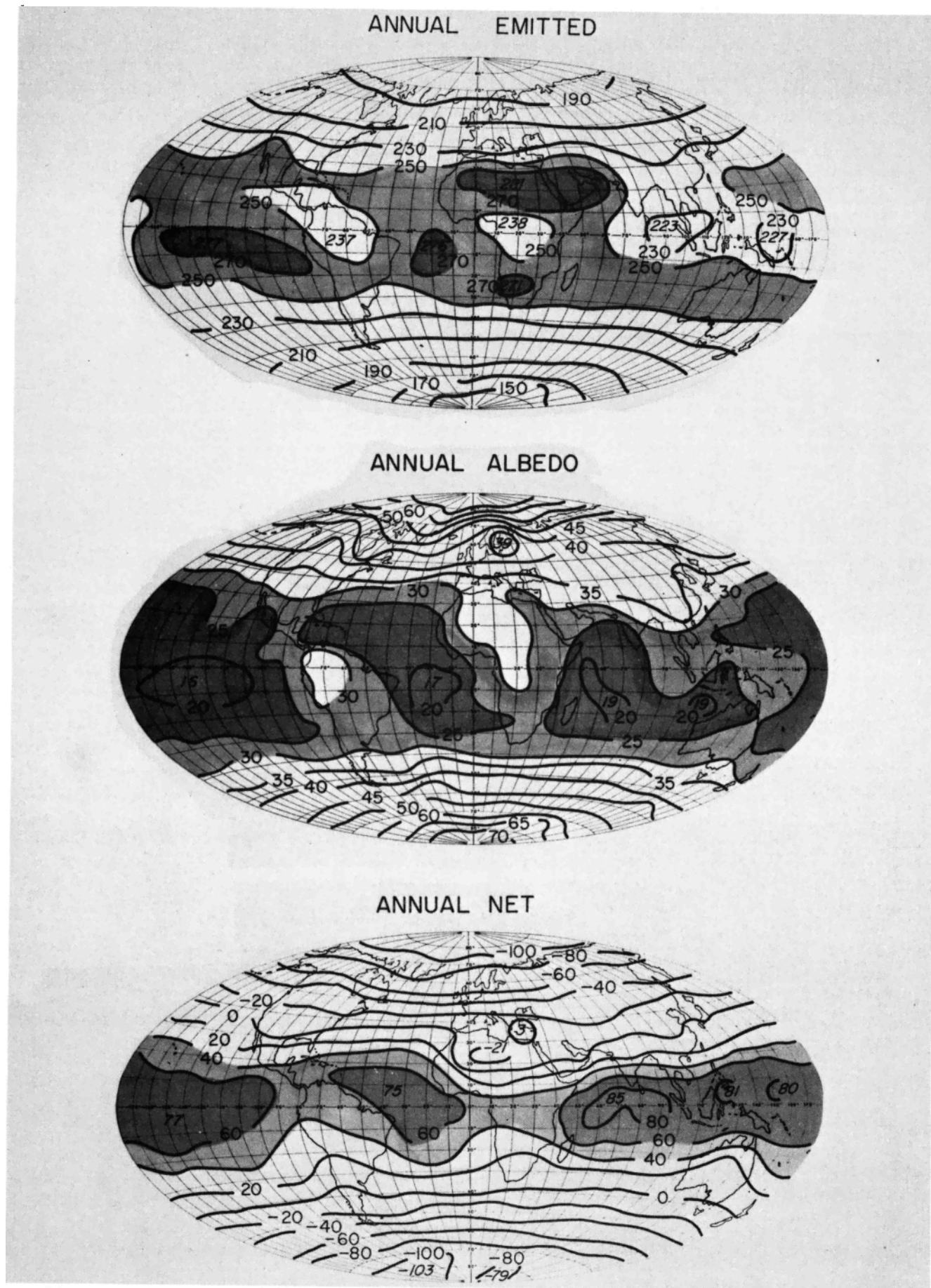


Fig. 6. Mean annual map of outgoing infrared radiation in W m^{-2} , planetary albedo (%), and net radiation (W m^{-2}) for the 48-month period.

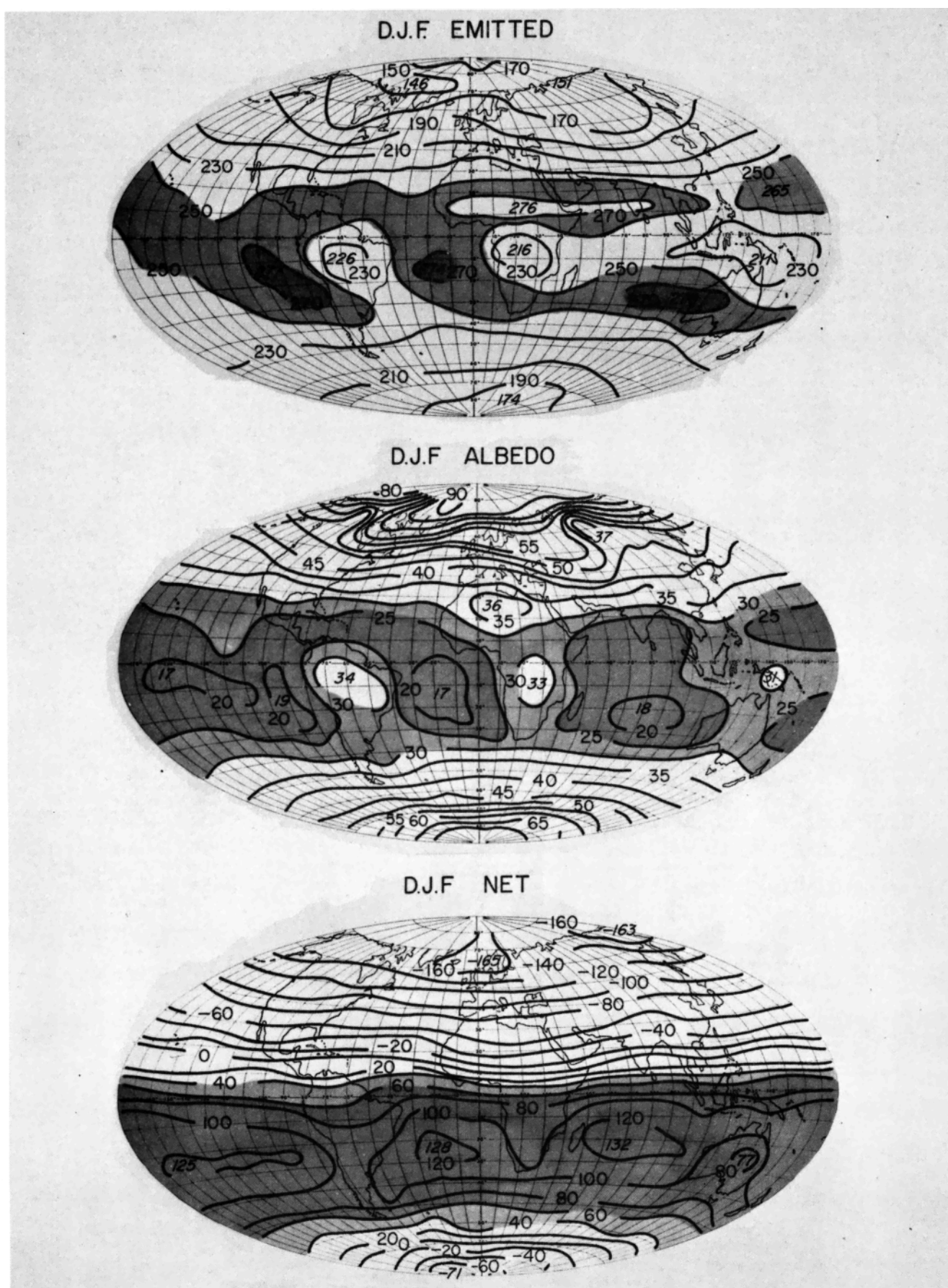


Fig. 7. Same as for Figure 6 but for the DJF season.

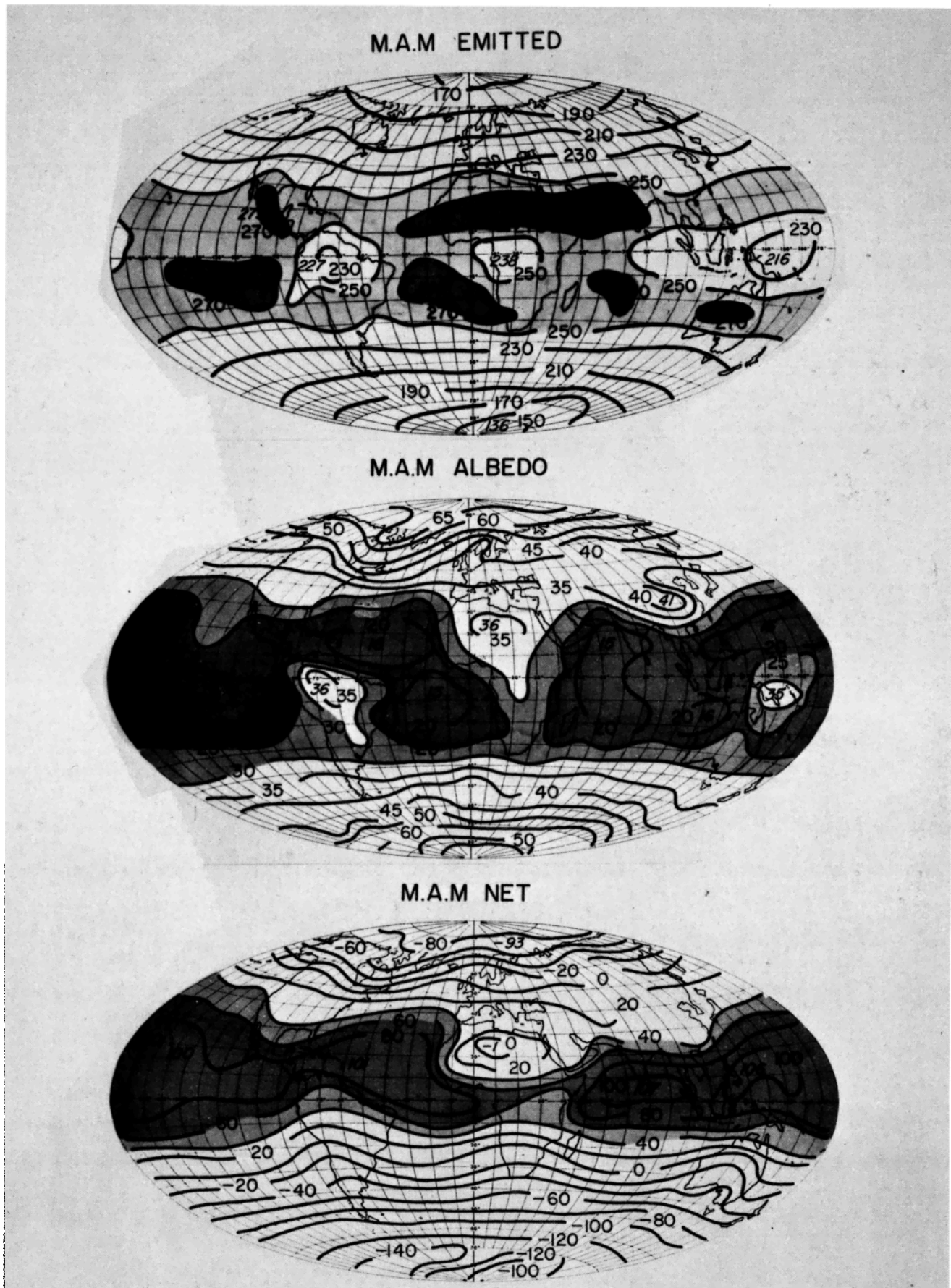
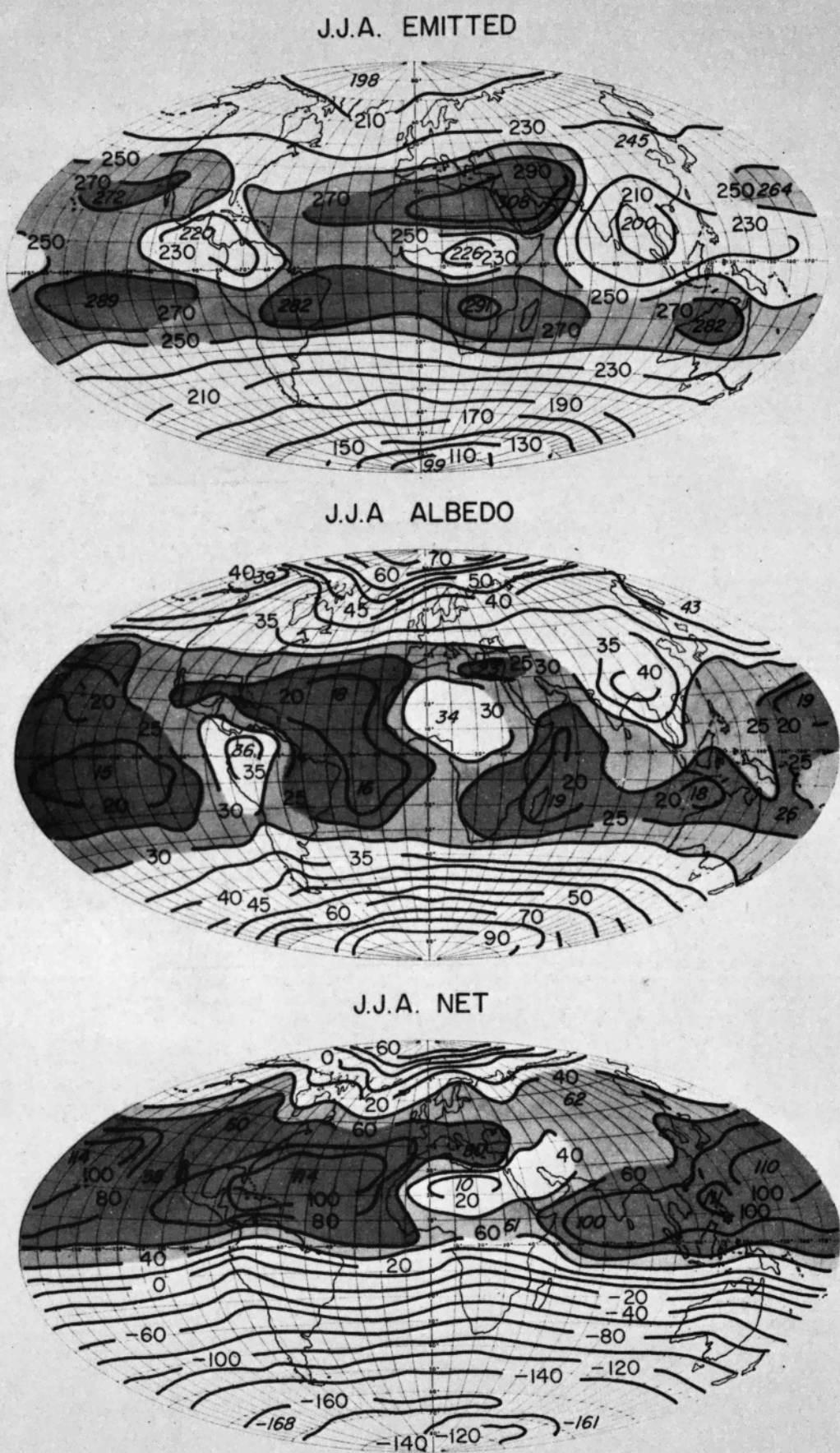


Fig. 8. Same as for Figure 6 but for the MAM season.



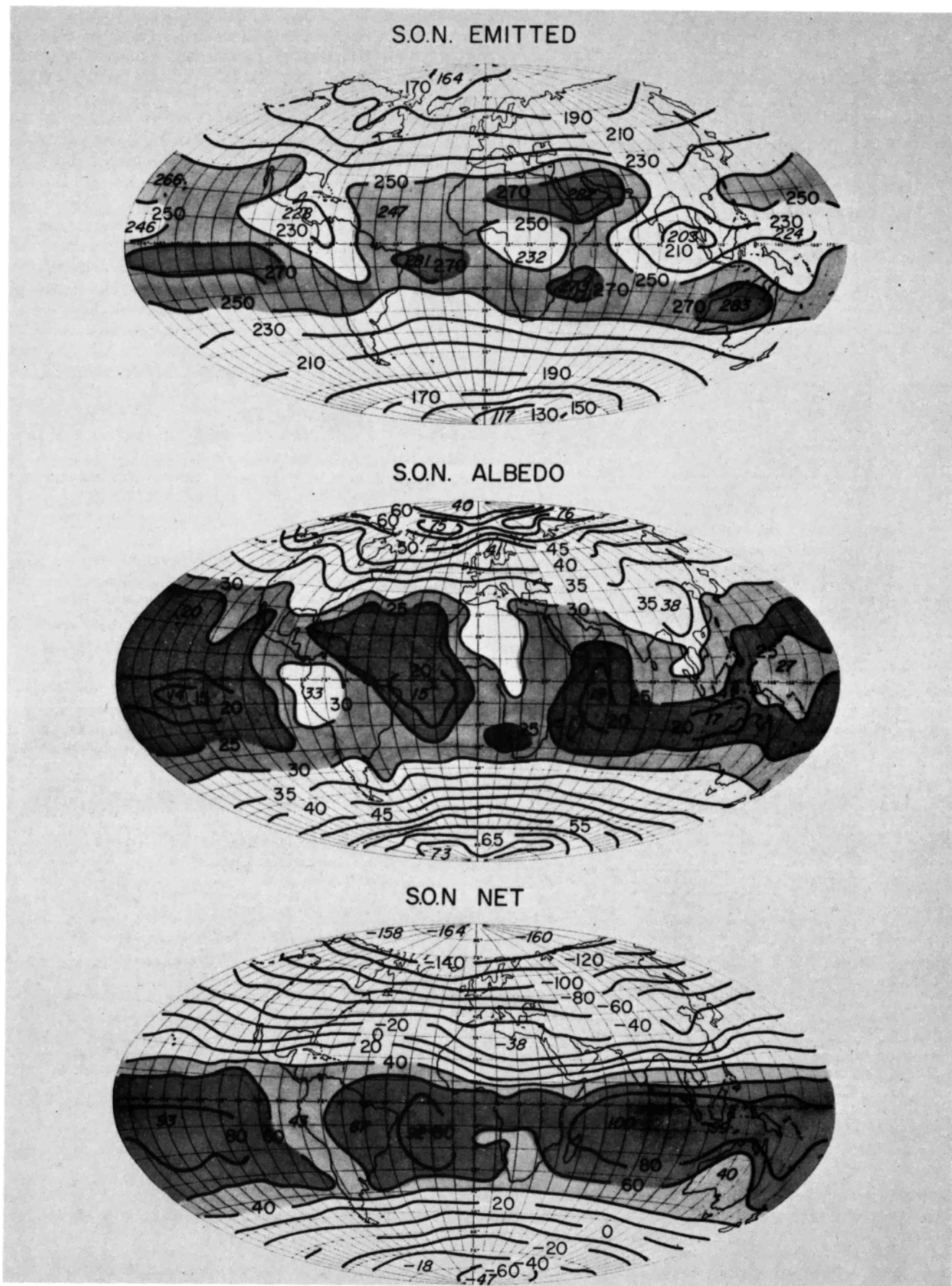


Fig. 10. Same as for Figure 6 but for the SON season.

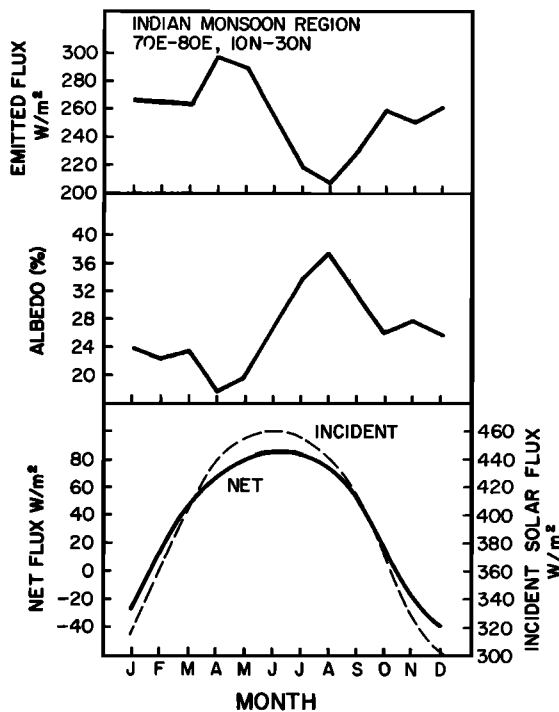


Fig. 11. The annual cycle of the planetary albedo, longwave flux to space, and net radiative flux for the Asian monsoonal region 70°E to 80°E and 10°N to 30°N . Superimposed on the net flux is the annual cycle of the incident solar flux at the top of the atmosphere (dashed curve).

13a and 13b is the percentage of the total variance explained by these cycles, the total variance being defined as the variance in the sample of 12 monthly maps. The amplitudes of the annual cycle are largest in the higher latitudes and can be attributed to the more dramatic change of solar elevation during the year. The amplitudes are smaller in the tropics with a

well-defined narrow belt of minimum values centered at the equator. The amplitudes of the semiannual cycle, on the other hand, displays a maximum equatorward of about 20° latitude (in part from the 'passage' of the sun) and also a distinct maximum in the polar regions.

The variance in the next flux, shown in Figures 12a and 12b, is almost completely explained (with a few percent or about 6 W m^{-2}) by the annual cycle poleward of about 20° latitude and the combined annual plus semiannual cycle equatorward of 20° . The variation of net flux largely arises from the changing input energy to the system and the extant energy composed of the emitted and reflected radiant fluxes remains roughly uniform in the mean with a mutual cancellation occurring between α and I . In a similar analysis of the monthly averaged mean zonal wind [\bar{u}], Oort and Rasmusson [1971] showed that 95% or more of the variance of [\bar{u}] could be explained by the annual plus semiannual cycles and that only a small amount of variation resides in the higher harmonics.

Figure 14a presents the amplitude of the annual cycle of emitted flux. A distinct ocean continent contrast is evident (particularly in the northern hemisphere) with generally smaller amplitudes over the ocean regions. This suggests that the oceans perhaps provide a stabilization of outgoing longwave radiation. There are three specific regions of large amplitudes, one centered over the Bay of Bengal, one west of Panama, and one centered near the Middle East. The large amplitudes over the monsoon regions are influenced by the variability cloud distributions in those regions.

Figures 14b and 14c show maps of the explained variance of the emitted flux and planetary albedo by the combined annual and semiannual cycles. These individual budget components show more higher frequency variance than the net flux discussed above. The variance of the emitted flux can largely be described in terms of the annual and semiannual cycles except in lower latitude regions. The unexplained vari-

N-AMPLITUDE (W m^{-2}) ANNUAL

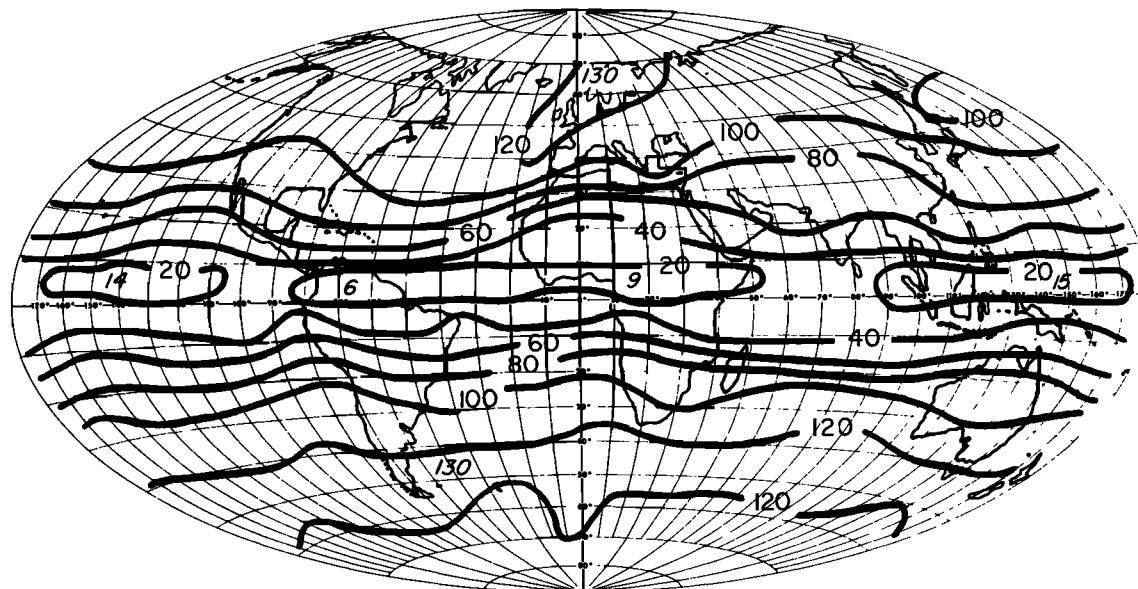


Fig. 12a

Fig. 12. The global distribution of amplitude (W m^{-2}) of (a) the annual and (b) semiannual oscillations in the net radiative flux.

**N-AMPLITUDE (W/m^2)
SEMI-ANNUAL**

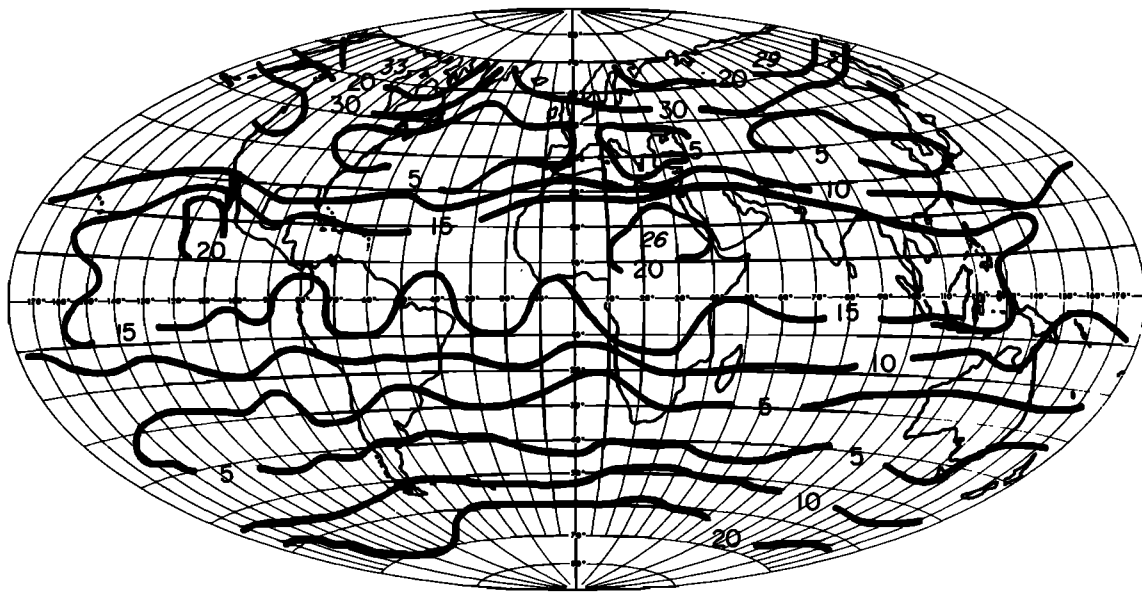


Fig. 12b

ability of planetary albedo, on the other hand, is much larger and is indicative of variations of higher frequency than either the annual or the semiannual cycles.

Crucial to the problem of climate is the estimation of year-to-year variations in the radiation budget to distinguish regions of possible large interannual variations that, potentially, are climatically most important. As a measure of the possible year-to-year variability in the radiation budgets, global distribution of dispersion was presented. Each individual monthly map was rescaled to the same 70°N to 70°S area average as an

attempt to remove most of the systematic inter-instrument differences portrayed in Figure 2.

Figures 15a and 15b show the global distribution of the relative dispersion of the emitted IR flux and planetary albedo determined from month-to-month variations in the 48 months of data summarized in Table 2. Figure 15c presents the dispersion of net flux defined as

$$\sigma(N) = \sum_{m=1}^{12} (1/12) \left[\frac{1}{J} \sum_{i=1}^J (N_{i,m} - \bar{N}_m)^2 \right]^{1/2} \quad (6)$$

N-EXPLAINED VARIANCE (%)

ANNUAL

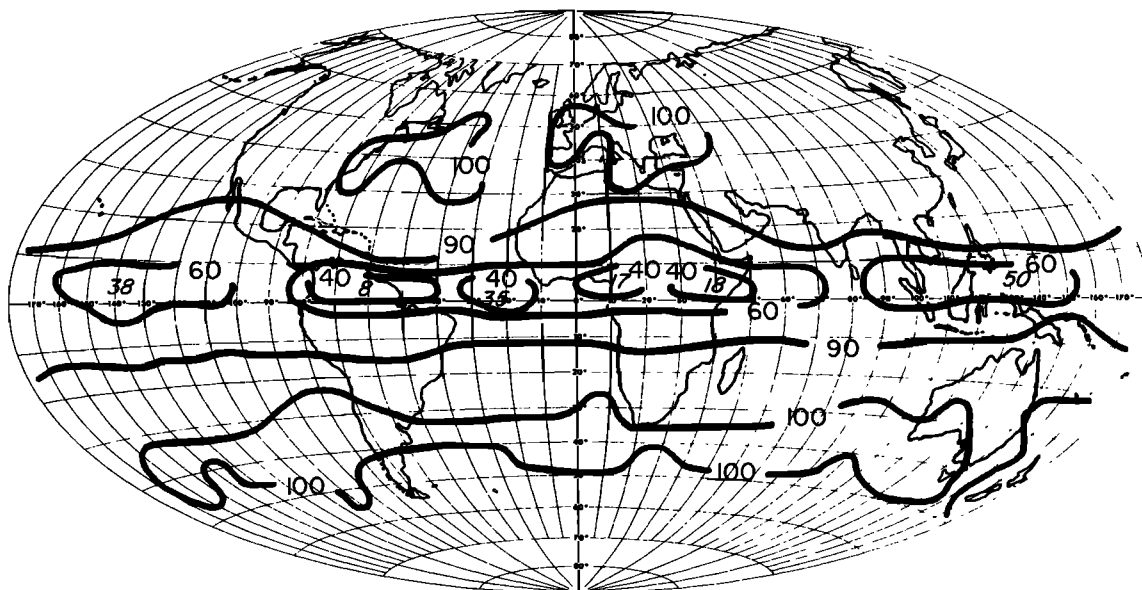


Fig. 13a

Fig. 13. The global distribution of the explained variance (%) of the (a) annual and (b) semiannual oscillations in the net radiative flux.

**N-EXPLAINED VARIANCE (%)
SEMI-ANNUAL**

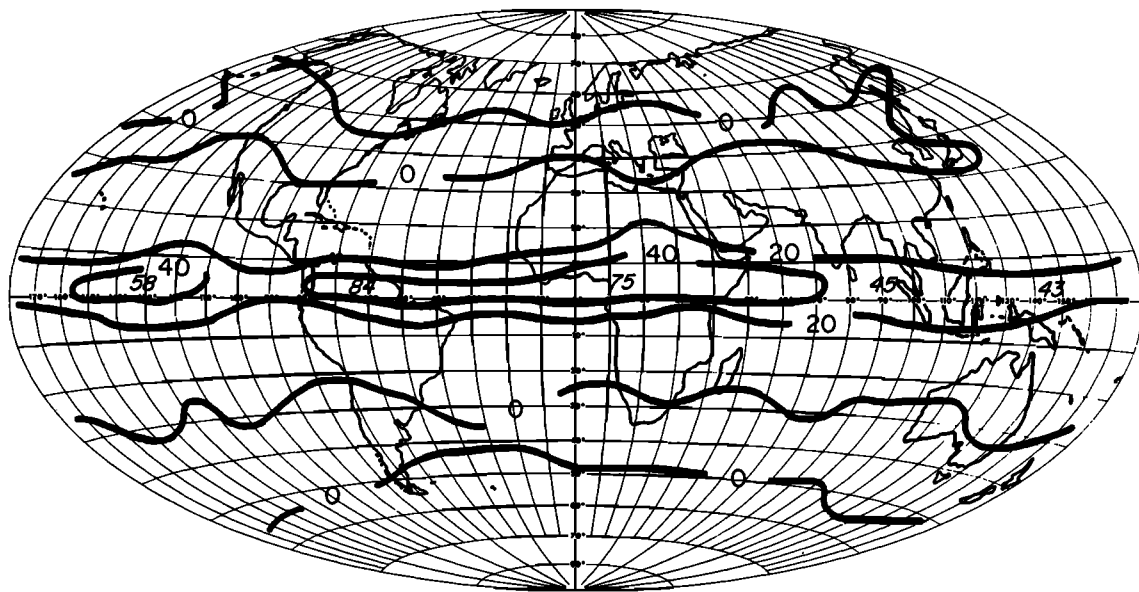


Fig. 13b

where $N_{i,m}$ is the individual mean monthly observation of net flux for the m th month, J is the number of such observations (~ 5 in this case), and \bar{N}_m is the mean monthly value determined from the J observations. The relative dispersions shown in Figures 15a and 15b are expressed as percentages of the mean annual value of the appropriate budget quantity. Whereas the statistics of Figures 12, 13, and 14 describe the variation of \bar{N}_m over the annual cycle, the analysis in the form of (6) provides an indication of the variability of an individual

month about the mean monthly value. Where this statistic is large, the variability of the relevant budget quantity is large.

The distribution of relative dispersion of IR emitted flux, as shown in Figure 15a, shows a distinct continental/ocean influence with larger variabilities occurring over land and generally smaller values over the oceans. Planetary albedo has relatively high relative dispersion. Figure 15b shows that the regions of most pronounced variability of albedo from one year to another occurs over the Asian monsoon region, in the

**I-AMPLITUDE (W/m²)
ANNUAL**

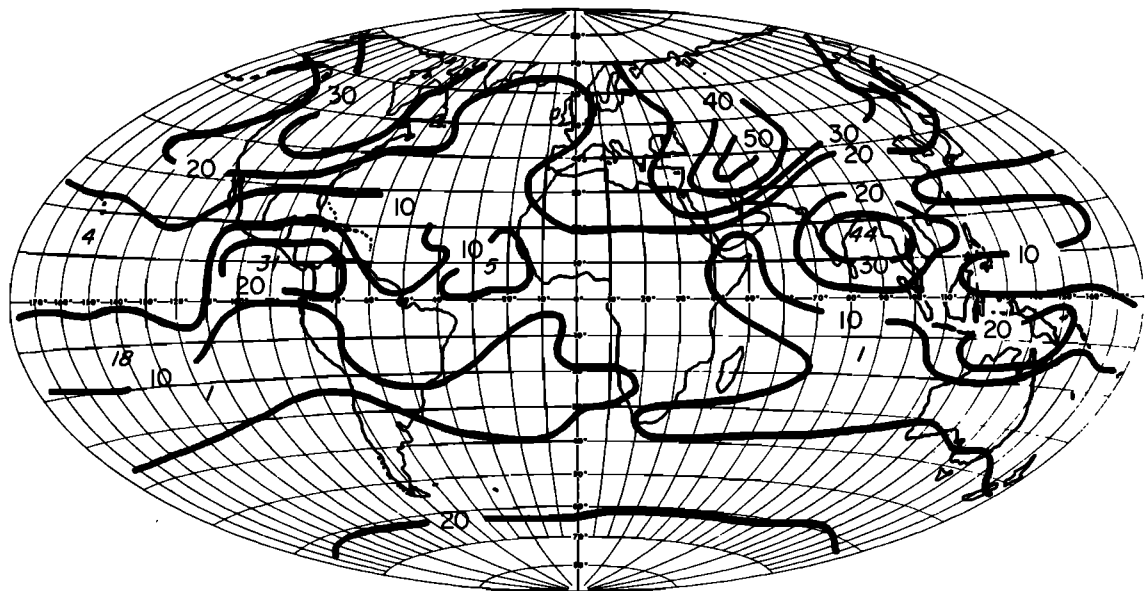


Fig. 14a

Fig. 14. The (a) amplitude (W m^{-2}) and the (b) explained variance (%) of the combined annual and semianual oscillations in the outgoing longwave flux. The (c) explained variance (%) of the combined annual and semianual oscillations in the planetary albedo.

I-EXPLAINED VARIANCE (%) ANNUAL+SEMI-ANNUAL

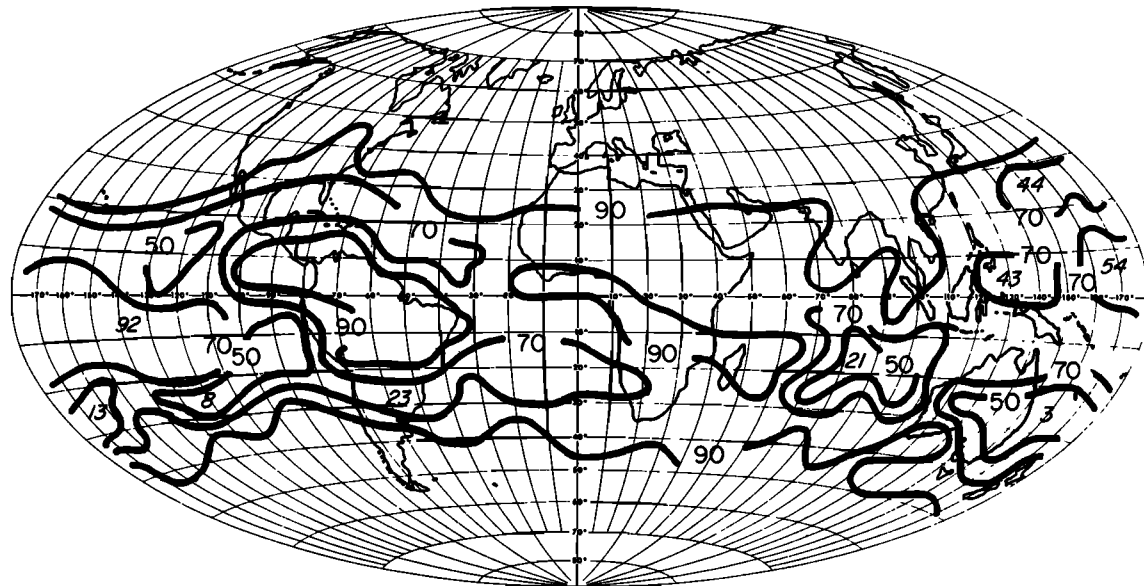


Fig. 14b

northern Pacific, west of South America, and over the Amazon basin with a coupled maximum east of the Gulf of Mexico. The large relative dispersion west of South America is associated with the variable extent of low stratiform cloud occurring in the subsidence regions over cold ocean currents. This variability is particularly accentuated since the annual mean albedos in this immediate region are small (see Figure 6b). The large variability of I and α over the Amazon basin can be attributed to the well-known rain/dry season, which markedly changes cloud patterns and is itself variable from one year to the next. The peripheries of the ITCZ and the Asian monsoon regions appear as regions of distinctly high

relative dispersion in emitted flux indicating that the extent of these circulation phenomena are quite variable.

The dispersion of net flux, shown in Figure 15c, indicates a pronounced variability of net radiation input over the Sahara desert. In this region the emitted flux and albedo are large, and relatively small changes in these quantities may appear as large changes in net flux. It is important to note that the magnitudes of the dispersion in some of the more variable regions are generally larger than 10 W m^{-2} and often as large as 20 W m^{-2} . These regions, for example over the Pacific east of Asia, the Asian monsoon region, the stratocumulus region west of South America, and the Sahara desert, among others, should

α - EXPLAINED VARIANCE (%)
ANNUAL+ SEMI-ANNUAL

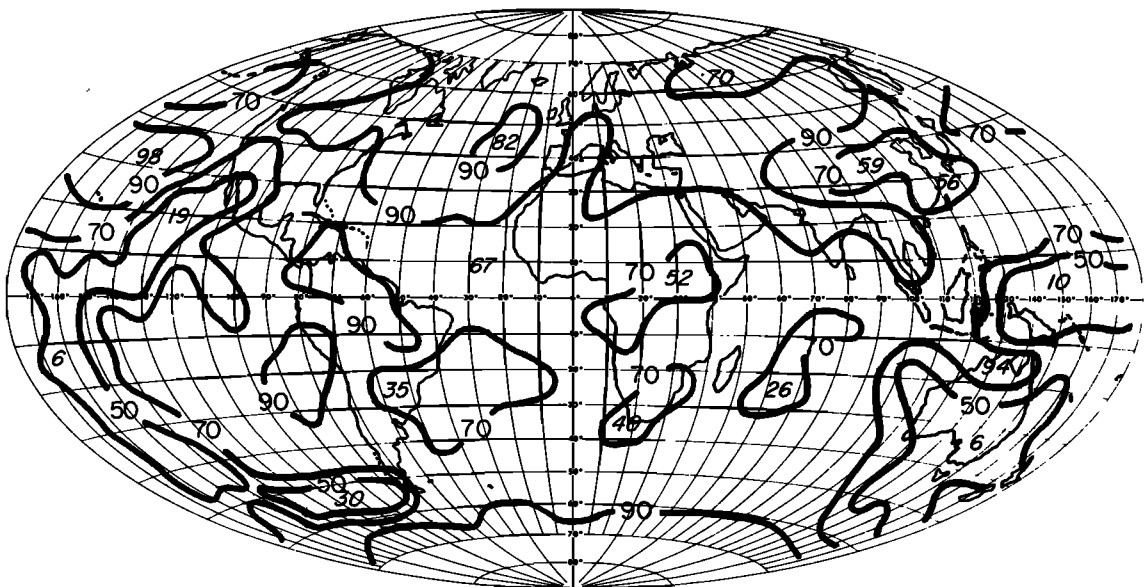
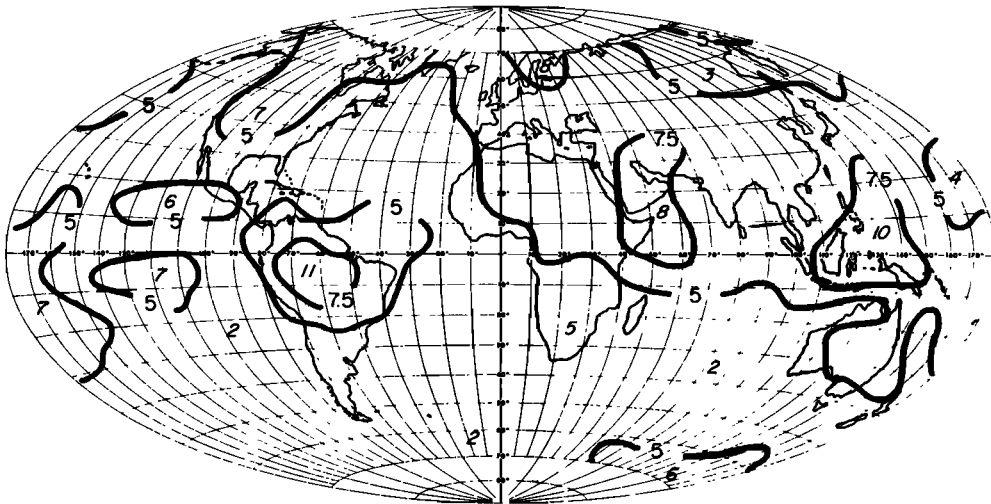


Fig. 14c

EMITTED

a. REL. DISPERSION (%) 48 months



ALBEDO

b. REL. DISPERSION (%) 48 months

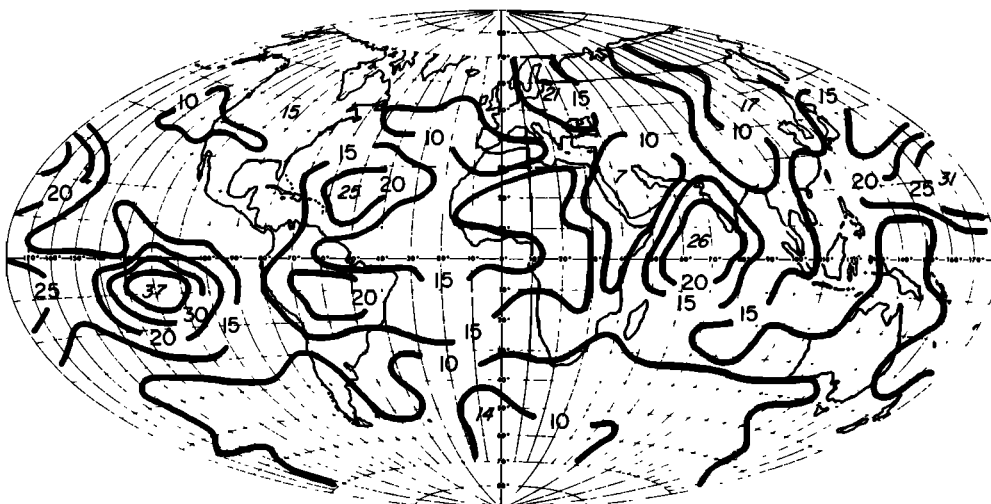
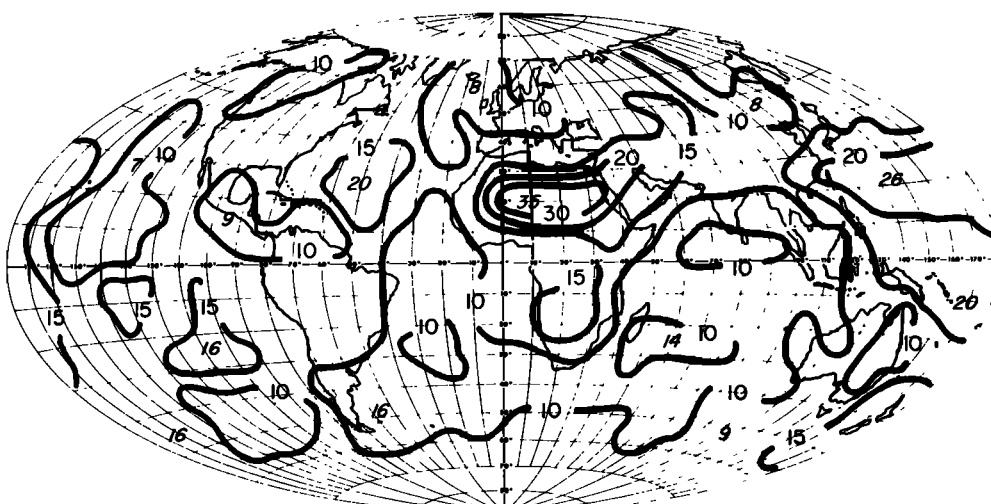
c. DISPERSION OF NET FLUX (W/m^2)

Fig. 15. The relative dispersion (%) of (a) outgoing longwave radiation and (b) planetary albedo determined from the 48 months of satellite data; (c) the dispersion (W m^{-2}) of net flux determined from the 48 months of data.

be the focus of radiation budget modeling studies, for here the impact on climate is potentially large.

4. MODEL INTERPRETATIONS OF THE RADIATIVE BUDGETS

The determination of the radiative balance at the earth's surface is essential to atmospheric modeling and prediction from climatic time scales down to those scales for which radiative heating is significant. Further, the radiative budget at the earth's surface is important for the understanding of the partitioning of poleward energy transports into its atmospheric and oceanic components. A radiative transfer model [adapted from *Stephens and Webster*, 1979] was employed to provide the surface radiative budgets, and the budgets determined at the top of the model atmosphere were verified by using the satellite data described above.

a. Radiative Transfer Model

The radiative transfer model for the determination of shortwave fluxes within the atmosphere is based largely on the scheme of *Stephens and Webster* [1979] that incorporates the clear sky parameterizations of *Lacis and Hansen* [1974]. The calculation of the shortwave fluxes within the atmosphere therefore include absorption by water vapor and ozone but none of the smaller absorption by CO₂ and O₃. For this particular study, the Stephens and Webster model is extended to $N=15$ layers.

The longwave fluxes from the cloud boundaries (exitances) are determined via the effective emittance approach, i.e.,

$$\begin{aligned} F^{\uparrow}(\text{cloud top}) &= F_0^{\uparrow}(1 - \epsilon^{\downarrow}) + \epsilon^{\downarrow}\sigma T_c^4 \\ F^{\downarrow}(\text{cloud base}) &= F_0^{\downarrow}(1 - \epsilon^{\downarrow}) + \epsilon^{\downarrow}\sigma T_c^4 \end{aligned} \quad (7)$$

where $F_0^{\downarrow,\uparrow}$ are the respective incident cloud top and base fluxes determined from the radiative transfer equation applicable to the clear sky layers above and below the specified cloud layer, viz

$$\begin{aligned} F^{\uparrow}(z) &= B(T_c)(1 - \epsilon^{\downarrow}(u)) + \int_0^u B(u') d\epsilon^{\downarrow}(u') \\ F^{\downarrow}(z) &= \int_u^\infty B(u') d\epsilon^{\downarrow}(u') \end{aligned} \quad (8)$$

where B is the black body function (in flux units) and u is the absorber amount for the path extending from the level of interest (z) to the appropriate boundary (ground, cloud base, or top of the atmosphere). Note that we have differentiated between upward and downward emittances, which were taken from *Rodgers* [1967] with the correction for the 'e type' absorption effect as discussed in *Stephens and Webster* [1979].

Thus the first term on the right-hand side of (7) represents the contribution to the exitance by the transmitted components of the incident flux, and the second term is the emitted component by the cloud layer with a temperature T_c . Thus (8) and (7) are coupled together with (8) determining the boundary fluxes at cloud top and base and (7) is applied to determine the exitant fluxes from the cloud.

An atmosphere with multiple cloud layers was treated in the same manner as by *Manabe and Strickler* [1964]. Simply, the flux at some level z above (say) three layers of cloud (high, middle, and low) was determined from the combination of

radiant fluxes determined for high, middle and low cloud separately. The resultant flux becomes

$$\begin{aligned} F_z^{\uparrow} &= F_{\text{clear}}^{\uparrow}(z)(1 - \Theta_l)(1 - \Theta_m)(1 - \Theta_h) + \Theta_l(1 - \Theta_m) \\ &\quad (1 - \Theta_h)F_{\text{low}}^{\uparrow}(z) + \Theta_m(1 - \Theta_h)F_{\text{mid}}^{\uparrow}(z) + \Theta_hF_{\text{high}}^{\uparrow}(z) \end{aligned} \quad (9)$$

where $\Theta_{l,m,h}$ are the low, middle, and high cloud amounts, respectively, and the fluxes with subscripts clear, low, middle, and high represent those fluxes at reference level z determined for clear sky and overcast sky conditions assuming low, middle and high cloud. A similar expression can be written for the downward fluxes.

A brief outline describing the method of incorporating the transmittance in the radiative transfer model is presented below.

Water vapor transmittance. The transmittance through the major water vapor absorption bands is incorporated in the model by using the temperature dependent gray body emissivity approach of *Rodgers* [1967] with the extension of *Stephens and Webster* [1979] to include the absorption in the atmospheric window region which is dependent on water vapor partial pressure ('e type absorption). The absorber amount assumed is corrected for pressure effects by employing the scaled formula

$$u = \int \frac{c(\phi)}{g} P_s \phi^{\alpha} d\phi \quad (10)$$

where $c(\phi)$ is the water vapor mixing ratio, P_s is the surface pressure, g is the acceleration under gravity, $\phi = P/P_s$, and α is chosen for the suitable absorption band. In this case, $\alpha = 0.9$ for the entire combined water vapor absorption. There is no theoretical justification for the one parameter scaling approach (10), but it is generally recognized that such a correction is better than none at all. Comparison of radiative transfer schemes employing this approach to those employing a higher order correction (the Curtis Godson approximation) show acceptably good agreement at least in the troposphere [*Stone and Manabe*, 1968]. This approach is likely to be reasonable for water vapor absorption in the troposphere but is not acceptable for CO₂ and O₃ absorption in the stratosphere.

Water vapor—CO₂ overlap (15 μm). The CO₂-water vapor overlap region is treated as a single interval 200 cm⁻¹ wide centered at 667 cm⁻¹ [after *Rodgers and Walshaw*, 1966]. The transmittance employed in the model is determined from the multiplication of the transmittance of each gas via

$$\tau_{\text{CO}_2, \text{H}_2\text{O}} = \tau_{\text{CO}_2} \times \tau_{\text{H}_2\text{O}} \quad (11)$$

This equation is valid provided the transmittance of each gas is expressed in a suitable form that preserves its multiplicative properties. The statistical band model (exponential in form) is applied to determine both $\tau_{\text{H}_2\text{O}}$ and τ_{CO_2} by using the published band model properties of *Rodgers and Walshaw* [1966].

Correction for pressure variations along the absorption path are performed by application of the Curtis Godson approximation, which defines a scaled absorber amount \bar{u} and a mean pressure $\bar{\phi}$ by

$$\begin{aligned} \bar{u} &= \int du \\ \bar{u}\bar{\phi} &= \int \phi du \end{aligned} \quad (12)$$

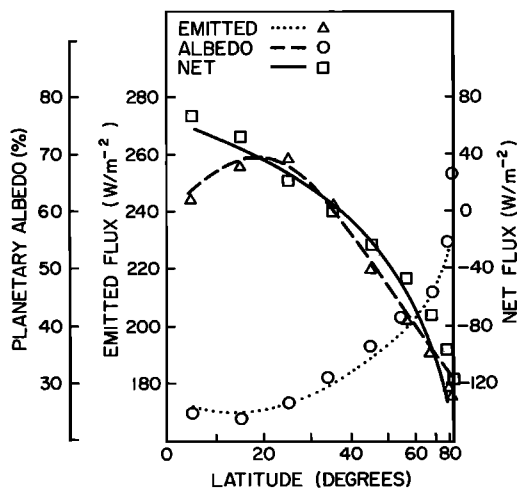


Fig. 16. Comparison of the theoretically calculated zonally averaged radiation budget quantities (dotted, dashed, and solid curves) to the values derived from satellite data (triangles, circles, and squares).

Transmission in the 9.6- μm ozone band. Neither the Goody random model (as employed above for the $\text{CO}_2\text{-H}_2\text{O}$ overlap) nor the Curtis Godson approximation adequately describe the absorption of IR radiation by ozone. The latter approximation can introduce substantial error to the transmittance estimates. A simple three parameter approximation (c.f. the two parameter Curtis Godson approximation) after Goody [1964] is included in the Malkmus [1967] random model [e.g., Rodgers, 1968]. The three parameter approximation is far more simple than that introduced by Kuriyan *et al.* [1977] and performs equally as well.

Cloud-radiative properties. The radiative properties of the various cloud types are selected in the following manner. Low and middle level clouds are assumed to be water clouds and their longwave and shortwave properties are determined from the parameterization of Stephens [1978]. The shortwave absorption and albedo are similarly estimated from that parameterization for the given solar zenith angles. The radiative properties are so derived for an assumed liquid water path of 140 g m^{-2} (i.e., for a cloud with a visible optical thickness of 39).

The reflectance emittance relation assumed in the present model is determined assuming the cloud albedo-liquid water path parameterization of Stephens [1978] for water clouds. The effective emittance-liquid (ice) water path (W) was adjusted as

$$\epsilon^{L\uparrow} = 1 - \exp(0.1 W) \quad (13)$$

for high cloud to make the combined reflectance emittance relation consistent with satellite-deduced observations of Platt *et al.* [1980].

The extent to which (13) is valid is difficult to determine, but it does agree well with the results derived from the observations of Cox and Griffith [1979].

b. Zonally Averaged Data

The following calculations were performed by using the zonally averaged fields of temperature and humidity published by Oort and Rasmussen [1971]. All other latitude-dependent parameters required by the model were taken from Ohring and Adler [1978] and the cloud amounts were adopted from Manabe [1969] who based his values on London [1957]. The

cloud position was also taken from Manabe, and the cloud was assumed to exist somewhere in the specified layer.

c. Simulation of Zonally Averaged Radiative Fields

In this section the model calculations of the radiative quantities employing the zonally averaged parameters described above are compared with observations and previous radiative budget calculations. The model radiative sources and sinks are a critical factor for any climate modeling exercise, and it should prove interesting to compare the present radiative budget calculations to past calculations particularly emphasizing discrepancy between the two.

Figure 16 shows the comparison of the zonally averaged profile of emitted flux, planetary albedo, and net flux as computed by the model and deduced from the satellite observations discussed above. Generally, the model calculations and the observed values agree closely. In particular, the variation of the radiation budget components with latitude is well handled, except for the albedo comparison in the polar regions. As mentioned above, the deduced albedos from satellite data require a significant correction for bidirectional reflectance, and the values in this region must be viewed with some caution.

Figures 17a and 17b show comparisons of the model calculations with London's [1957] radiative budget calculations of surface absorption of shortwave radiation and net flux of longwave radiation, respectively. The shortwave energy absorbed at the earth's surface calculated by the present model is generally larger than those of London. For example, at 15°N the computed solar radiation reflected to space is 26%; absorbed in the atmosphere, 17%; and absorbed in the ocean, 57%. These may be compared to those of London with estimates of 34, 14, and 52%. The differences are consistent with the findings of Vonder Haar and Hansen [1969], who found, from observational evidence, that the amount of shortwave radiant energy absorbed at the surface in tropical regions is 61% with reflected and absorbed amounts of 24 and 14%, respectively.

The net longwave fluxes at the surface as calculated by the present model are significantly smaller in low latitude regions

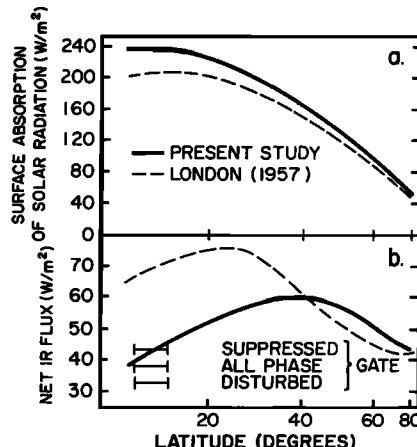


Fig. 17. Comparison of the surface radiation budget parameters (absorbed solar radiation and net IR flux from the surface) in W m^{-2} for the present set of calculations (solid curves) to the calculations of London [1957]. Included with the longwave budget are the budget values measured during the three stages of GATE indicated and averaged over the A array.

than those of London. The solid bars included on the diagram are the values obtained from measurements during the disturbed, undisturbed, and all phases of the GARP Atlantic Tropical Experiment (GATE). The GATE results suggest that the net flux of longwave radiation at the surface is fairly invariant over the highly opaque tropical atmosphere. It is therefore possible to compare meaningfully the model calculations employing annual mean profiles of moisture and temperature in tropical regions with the measurements from GATE.

The discrepancies that exist between the current model calculations (and observations) and those previously estimated from budget calculations are a direct result of the inclusion of additional absorption in the 8–14 μm window region by a water vapor partial pressure dependent absorption mechanism. The presence of this absorption has been realized since the early 1970's [Bignell, 1970, among others]. The effect of including this absorption produces a major increase in longwave cooling rates in the lowest levels of the tropical atmosphere. These changes, which are as large or larger than 2°C/day [Stephens, 1976] agree closely with the observed profile [e.g., Cox, 1969], which first indicated anomalous cooling in the lowest levels of the tropical atmosphere. The comparison presented in Figure 17b further illustrates such agreement between observation and theoretical calculation. The mechanism for this absorption is still open to debate with favored explanations relying on the existence of a water dimer molecule [e.g., Montgomery, 1978].

Despite the acceptance of the existence of this enhanced absorption, it has not been fully recognized in meteorological studies [Burroughs, 1979]. It is evident from Figure 17b that the resulting increased atmospheric emission supplies significantly more energy to the surface in the tropics than previously estimated. As a result, the excess energy available for transport toward the poles in the oceans or the air-sea interface energy exchange must be larger than hitherto assumed. These considerations are of prime importance for climate studies, and numerical models designed to simulate atmospheric circulations must be concerned with including this radiative process.

5. SUMMARY AND CONCLUSIONS

This paper presents the earth atmosphere radiation budgets derived from satellite observations for both seasonal and annual averages. The budgets are derived from a composite of 48 monthly mean radiation budget maps and represents a continuing compilation first reported by Vonder Haar and Suomi [1971]. The broad features presented in this paper for the annual average are similar to those reported earlier. The annual globally averaged emitted flux is 234 W m^{-2} , the planetary albedo is 0.30, and the net flux is zero, at least within measurement uncertainty. Also, the annual and season zonally averaged profiles of net flux show the predictable net energy input to the lower latitudes and net energy loss at higher latitudes, thus providing the differential heating between the equator and poles that must be balanced by the attendant poleward transport of heat by the atmosphere and ocean.

The globally averaged net flux displays an annual cycle that has a similar phase and magnitude to the annual cycle imposed on the solar input into the atmosphere by the externally forcings associated with earth sun geometry. A study of the geographic distribution of the mean variability (defined as the

total variance determined from the individual mean monthly data) of net flux reveals that generally greater than 95% of this variability can be explained in terms of semi and annual cycles most likely imposed by the regular earth-sun geometry variations throughout the year. The individual components of emitted flux and planetary albedo display more high frequency variability, particularly equatorward of about 30° latitude. In these regions the spatial and temporal scales of albedo are dominated by cloud-free oceans and cloudy and desert area differences, and thus the albedo is likely to display some high frequency variability governed by cloud distributions in particular. The variability of emitted flux, on the other hand, is governed by regions of cloud free (including low cloud) and very high cloud, particularly convective cloud zones, and as a result is less variable than albedo. Except in regions over deserts and low cloud, these albedos are negatively correlated with emitted flux. This reciprocity is due to the cloud influence on emitted and reflected fluxes and occurs such that the total average upwelling flux from the earth atmosphere system remains more or less uniform. While the mean annual variation of the radiative budget quantities is strongly forced by the solar radiation input, the variability of the radiation budget from one year to the next is shown to be large. These regions, for example, over the Pacific east of Asia, the Asian monsoon region, the stratocumulus region east of South America, and the Saharan desert should be the focus of radiation budget studies, for here the impact on climate is potentially large.

Radiative transfer simulations of the observed budget quantities, at least for the zonally averaged case, are good. The inclusion in the model of enhanced absorption in the 8–14 μm window region by a proposed water vapor dimer results in some 35 W m^{-2} more radiant energy absorbed by the oceans in the tropics than previously estimated. The validity of this result was verified by using results from the GATE radiation budget measurements. As a result, this excess energy input into the oceans in lower latitudes must result in larger poleward heat transports by the oceans or air-sea interface energy exchanges. It was shown that the changes of the emitted and reflected fluxes, largely due to cloud distribution variations, often negatively correlate such that the cloud signal in the net flux is often small. Furthermore, the annual variability of net flux can be predominantly explained in terms of a semi-annual and annual cycle perhaps imposed by the influence on solar radiation input through the regular change in solar declination throughout the year. Thus the annual variation of net flux can be successfully modeled in terms of the rather simple earth-sun geometry requirements and with seasonally invariant cloud cover. However, this may overlook major climate impact areas of poor radiation reciprocity such as land deserts, stratus regimes, and cirrus areas as well as the variability of the net flux of one season from year to year. Furthermore, the general treatment does not ensure that either the surface radiation budgets or the atmospheric heating are modeled adequately. It is the latter quantity that provides the only radiative influence on the rest of the model dynamics; neither does it ensure that areas of high variability in radiation exchange with space, areas of potentially high climatic impact, are represented properly.

Acknowledgments. This research was supported by the Langley Research Center, NASA, under contract NAS1-15553 to the Research Institute of Colorado. We thank L. Parkinson and D. Clark for clerical assistance.

cal assistance and M. Howes for drafting the figures. Eric Smith provided his GATE results for comparison. We would also especially like to acknowledge A. Oort for his valuable discussions, particularly concerning the discussion of variances.

REFERENCES

- Bignell, K. J., The water vapour infrared continuum, *Q. J. R. Meteorol. Soc.*, 96, 390–403, 1970.
- Burroughs, W. J., The water dimer: A meteorologically important molecular species, *Weather*, 34, 233–236, 1979.
- Campbell, G. G., and T. H. Vonder Haar, Climatology of radiation budget measurements from satellites, *Atmos. Sci. Pap.* 322, Colo. State Univ., Fort Collins, Colo., 1980.
- Charney, J., Dynamics of deserts and droughts in the Sahel, *Q. J. R. Meteorol. Soc.*, 101, 193–202, 1975.
- Cox, S. K., Observational evidence of anomalous infrared cooling in a clear tropical atmosphere, *J. Atmos. Sci.*, 26, 1347–1349, 1969.
- Cox, S. K., and K. T. Griffith, Estimates of radiative divergence during phase III of GATE, I, Methodology, *J. Atmos. Sci.*, 36, 566–575, 1979.
- Ellis, J. S., and T. H. Vonder Haar, Zonal average earth radiation budget measurements from satellites for climate studies, *Atmos. Sci. Pap.* 240, Colo. State Univ., Fort Collins, Colo., 1976.
- Ellis, J. S., T. H. Vonder Haar, S. Levitus, and A. H. Oort, The annual variation in the global heat balance of the earth, *J. Geophys. Res.*, 84, 1958–1962, 1978.
- Goody, R. M., The transmission of radiation through an inhomogeneous atmosphere, *J. Atmos. Sci.*, 21, 575–581, 1964.
- Gruber, A., and J. S. Winston, Earth-atmosphere radiative heating based on NOAA scanning radiometer measurements, *Bull. Am. Meteorol. Soc.*, 59, 1570–1573, 1978.
- Hickey, J., L. Stowe, H. Jacobowitz, P. Pelegrino, R. Maschoff, A. Arking, J. House, A. Ingersoll, and T. H. Vonder Haar, Initial solar irradiance determination from Nimbus 7 cavity radiometer measurements, *Science*, 208, 281–283, 1980.
- Kuriyan, J. G., Shippony, and S. K. Mitra, Transmission function for IR radiative transfer in an inhomogeneous atmosphere, *Q. J. R. Meteorol. Soc.*, 103, 511–517, 1977.
- Lacis, A., and J. G. Hansen, A parameterization for the absorption of solar radiation in the earth's atmosphere, *J. Atmos. Sci.*, 31, 118–133, 1974.
- Liou, K. N., A numerical experiment on Chandrasekhar's discrete-ordinate method for radiative transfer: Applications to cloudy and hazy atmospheres, *J. Atmos. Sci.*, 30, 1303–1326, 1973.
- London, J., A study of the atmospheric heat balance, final report, Coll. of Eng. Res. Div., New York Univ., New York, 1957.
- McKee, T., and S. K. Cox, Simulated radiance patterns for finite cubic clouds, *J. Atmos. Sci.*, 33, 2014–2020, 1976.
- Malkmus, W., Random Lorentz band model with exponential tailed S^{-1} line intensity distribution function, *J. Opt. Soc. Am.*, 57, 323–329, 1967.
- Manabe, S., Climate and the ocean circulation, I, The atmospheric circulation and the hydrology of the earth's surface, *Mon. Weather Rev.*, 97, 739–774, 1969.
- Manabe, S., and R. F. Strickler, Thermal equilibrium of an atmosphere with a convective adjustment, *J. Atmos. Sci.*, 21, 361–385, 1964.
- Montgomery, G. P., Temperature dependence of infrared absorption of water vapor near 1200 cm^{-1} , *Appl. Opt.*, 17, 2299–2303, 1978.
- Ohring, G., and S. Adler, Some experiments with a zonally averaged climate model, *J. Atmos. Sci.*, 35, 186–205, 1978.
- Oort, A. H., and E. M. Rasmusson, Atmospheric circulation statistics, *Prof. Pap.* 5, Nat. Oceanic and Atmos. Admin., Washington, D. C., 1971.
- Oort, A. H., and T. H. Vonder Haar, On the observed annual cycle in the ocean-atmosphere heat balance over the Northern Hemisphere, *J. Phys. Ocean.*, 6, 781–800, 1976.
- Platt, C. M. R., D. Reynolds, and N. Abshire, Albedo of cirrus-inferences from groundbased lidar and geostationary satellite observations, *Mon. Weather Rev.*, 108, 195–204, 1980.
- Raschke, E., and W. R. Bandeen, The radiation balance of the planet Earth from radiation measurements of the satellite Nimbus 2, *J. Appl. Meteorol.*, 9, 215–238, 1970.
- Raschke, E., T. H. Vonder Haar, W. R. Bandeen, and M. Pasternak, The annual radiation balance of the Earth-Atmosphere system during 1969–70 from Nimbus 3 measurements, *J. Atmos. Sci.*, 30, 341–364, 1973.
- Riehl, H., and A. Miller, Differences between morning and evening temperatures of cloud tops over tropical continents and oceans, *Q. J. R. Meteorol. Soc.*, 104, 757–764, 1978.
- Rodgers, C. D., The use of emissivity in atmospheric radiation calculations, *Q. J. R. Meteorol. Soc.*, 93, 45–54, 1967.
- Rodgers, C. D., Some extensions and applications of the new random model for molecular band transmission, *Q. J. R. Meteorol. Soc.*, 94, 99–102, 1968.
- Rodgers, C. D., and C. D. Walsh, The computation of infrared cooling rates in planetary atmospheres, *Q. J. R. Meteorol. Soc.*, 92, 67–92, 1966.
- Short, D. A., and W. M. Wallace, Satellite inferred morning to evening cloudiness changes, *Mon. Weather Rev.*, 108, 1160–1169, 1980.
- Stephens, G. L., An improved estimate of IR cooling in the atmospheric window region, *J. Atmos. Sci.*, 33, 806–809, 1976.
- Stephens, G. L., Radiative properties of extended water clouds, II, Parameterizations, *J. Atmos. Sci.*, 35, 2123–2132, 1978.
- Stephens, G. L., Radiative transfer on a linear lattice: Application to anisotropic ice crystal clouds, *J. Atmos. Sci.*, 37, 2095–2104, 1980.
- Stephens, G. L., and P. J. Webster, Sensitivity of radiative forcing to variable cloud and moisture, *J. Atmos. Sci.*, 36, 1542–1556, 1979.
- Stone, H. M., and S. Manabe, Comparison among various numerical models designed for computing infrared cooling, *Mon. Weather Rev.*, 96, 735–741, 1968.
- Vonder Haar, T. H., and K. Hansen, Absorption of solar radiation in tropical regions, *J. Atmos. Sci.*, 26, 652–655, 1969.
- Vonder Haar, T. H., and V. Suomi, Measurements of the Earth's radiation budget from satellites during a 5 year period, I, Extended time and space means, *J. Atmos. Sci.*, 28, 305–314, 1971.
- Welch, R. M., S. K. Cox, and J. Davis, Solar radiation and clouds, *Meteorol. Monogr.*, 39, 1980.
- Winston, J. S., Planetary scale characteristics of monthly mean long-wave radiation and albedo and some year to year variations, *Mon. Weather Rev.*, 95, 235–256, 1967.
- Wiscombe, W. J., and S. G. Warren, A model for the spectral albedo of snow, I, Pure snow, *J. Atmos. Sci.*, 37, 2712–2733, 1980.

(Received March 26, 1980;
revised March 18, 1981;
accepted March 24, 1981.)